



Wavelet transformation based multi-time scaling method for crystal plasticity FE simulations under cyclic loading

Deepu S. Joseph¹, Pritam Chakraborty¹, Somnath Ghosh^{*2}

Department of Mechanical Engineering, The Ohio State University, Scott Laboratory, 201 West 19th Avenue, Columbus, OH 43210, USA

ARTICLE INFO

Article history:

Received 30 December 2009

Accepted 17 March 2010

Available online 31 March 2010

Keywords:

Crystal plasticity

Multi-time scaling

Wavelet transformation

Adaptivity

ABSTRACT

Microstructure based mechanistic calculations, coupled with physically motivated crack initiation criterion, can provide effective means to predict fatigue cracking in polycrystalline materials. However the accommodation of large number of cycles to failure, as observed in the experiments, could be computationally exhaustive to simulate using conventional single time scale finite element analysis. To meet this challenging requirement, a novel wavelet transformation based multi-time scaling algorithm is proposed for accelerated crystal plasticity finite element simulations in this paper. An advantage over other conventional methods that fail because of assumptions of periodicity etc., is that no assumption of scale separation is needed with this method. The wavelet decomposition naturally retains the high frequency response through the wavelet basis functions and transforms the low frequency material response into a “cycle scale” problem with monotonic evolution. The method significantly enhances the computational efficiency in comparison with conventional single time scale integration methods. Adaptivity conditions are also developed for this algorithm to improve accuracy and efficiency. Numerical examples for validating the multi-scaling algorithm are executed for a one dimensional viscoplastic problem and a 3D crystal plasticity model of polycrystalline Ti alloy under the cyclic loading conditions.

© 2010 Elsevier B.V. All rights reserved.

1. Introduction

Many metals and alloys, such as titanium alloys and Ni-base superalloys, find widespread utilization in various high performance applications e.g. in the automotive and aerospace sectors. During service, these materials are exposed to cyclic loading conditions due to start up and shut down processes or load reversals. In many cases, this results in their fatigue or time delayed fracture. Fatigue failure in the microstructure evolves in three stages [1], viz. (i) crack nucleation due to inhomogeneous plastic flow or grain boundary failure, (ii) subsequent crack growth by cyclic stresses, and (iii) coalescence of cracks to cause fast crack propagation.

A large body of literature exists in the field of fatigue of metals [1–5]. Fatigue analysis by total life approaches includes (i) the stress–life or S–N approach, where the stress amplitude versus life is determined, and (ii) the strain–life approach e.g. the Coffin–Manson rule, where the number of cycles to failure is determined as a function of plastic strain. The total life approaches have been adjusted for notch effects using fatigue strength reduction and for variable amplitude fatigue e.g. in the Palmgren–Miner rule of cumulative damage. In these cases,

microstructural effects are merely represented by shifts in such data curves after extensive testing. Alternatively, the defect or damage tolerance approaches determine fatigue life as the number of cycles to propagate a crack from a certain initial size to a critical size. These are determined from threshold stress intensity, fracture toughness, limit load, allowable strain or allowable compliance. The models assume the presence of a flaw in the structure, and predict life using models such as the Paris law [6]. Fatigue crack advance has been conventionally based on linear elastic fracture mechanics analysis related to the concepts of similitude. While these widely used models have worked well for alloys under specific test conditions, there is significant scatter in their predictions. The safe life and fatigue design criteria, conventionally employed in current practice [7], lead to premature retiring of a great number of expensive parts even before damage initiation, thus shortening their full useful life.

Lack of information on the material microstructure along with incorporation of underlying physics based mechanisms, prevent the creation of a generalized framework for conventional fatigue models to be applied to a variety of materials and loading conditions. Additionally, the lack of this information also results in a large scatter in the predicted life. Experimental studies on fatigue behavior of commercial alloys in [8–10] have demonstrated the influence of material deformation and damage mechanisms, creep, oxidation and microstructural instabilities on cyclic life. Morphological and crystallographic characteristics of the microstructure, e.g. crystal orientations

* Corresponding author.

E-mail address: ghosh.5@osu.edu (S. Ghosh).

¹ Graduate student.

² John B. Nordholt Professor.

and misorientations, grain size, grain boundary geometry etc., play significant roles in the mechanical behavior and fatigue failure response of the material. To account for these factors, the recent years have seen a paradigm shift towards the use of mechanistic models of detailed material microstructures for predicting fatigue crack nucleation and propagation. These methods show significant promise as superior alternatives to the empirical models. Many of these mechanistic approaches seek accurate description of material behavior through crystal plasticity based finite element models. Crystal plasticity theories with explicit grain structures are effective in predicting localized cyclic plastic strains [11–14]. Deformation modeling with crystal plasticity [15] has established that preferred grain orientations due to crystal rotation facilitate slip transmittal across grain boundaries and are a dominant cause for material flow anisotropy leading to failure. In crystal plasticity based modeling approaches, the mechanical response of polycrystalline aggregates are deduced from the behavior of constituent crystal grains with specific assumptions about their interaction. Computational studies, e.g. in [16–20] have modeled anisotropy and its evolution in large deformation processes with this approach. Significant efforts are currently being made in cyclic plasticity and fatigue modeling from microstructural stress–strain evolution. Finite element calculations have shown that depending on the loading conditions, significant gradients of stresses or strains can evolve, even within a single slip system. The mechanical behavior of aluminum alloys in cyclic loading using crystal plasticity based FEM simulations of crystalline aggregates have been investigated in [21,22]. In [12], the authors have incorporated a crystal plasticity model with kinematic hardening to model cyclic plasticity in high cycle fatigue of Ti alloys. Ghosh et al. [23–27] have developed crystal plasticity models for deformation and creep in titanium alloys, e.g. Ti-6Al and Ti-6242, along with associated crack nucleation under cyclic loading in [13,14,28]. They have also modeled deformation and ratcheting fatigue of HSLA steels in [29,30]. These calculations provide a platform for the implementation of physics based cyclic deformation and crack evolution criterion that accounts for the effects of microstructural inhomogeneities.

Typically fatigue life in metallic materials could be of the order of thousands of cycles, depending on the material and loading conditions. A major challenge with the crystal plasticity finite element simulations for fatigue life prediction is the accommodation of the large number of cycles to failure, or even crack nucleation. In single time-scale finite element solutions using conventional time integration algorithms [31,32], each cycle is discretized into an appropriate number of time steps, over which integration is performed. In crystal plasticity calculations, a high resolution in the time steps is required for each cycle throughout the loading process, often leading to exorbitant computational requirements. Consequently, many studies on cyclic deformation with 3D crystal plasticity [12,21,22,30] have resorted to simulating a small number of cycles (~100) and subsequently extrapolating the results to thousands of cycles for making fatigue life predictions. Extrapolation can lead to considerable error, particularly when it comes to the evolution of microstructural variables that are used in predicting local failure. It is therefore desirable to conduct simulations for a large number of cycles to reach the local states of crack nucleation and growth.

This requirement presents significant challenges due to the existence of different time scales, ranging from the scale of each load cycle to that of the life of the component. Methods of multi-scaling in the temporal domain may be introduced to avert some of these challenges. The method of direct separation of motions has been traditionally used to study the vibratory response under the application of high frequency loads [33,34]. It involves defining two separate integro-differential equations, one each for the high and low frequency components of the response. The high frequency component is either approximated or is calculated explicitly and is used in the integro-differential equation for the low frequency response. This

method is based on the assumption that all variables are either locally periodic or nearly periodic in the temporal domain and applications of similar methods have been made to material problems in e.g. [35,36]. These methods implicitly assume that scale separation is admitted in these problems. However, these methods cannot be extended to crystal plasticity solutions due to the strong non-periodic response of evolving plastic variables and also due to localization in the spatial domain. In addition, these methods often invoke two-way coupling between the time scales that requires having to solve initial value problems in each step at both time scales. This can result in very high computational time and may not provide any advantage over single time scale calculations. In [37], cyclic averaging in conjunction with asymptotic expansion of variables in the time domain has been proposed as a basis of multi-time scaling. However, asymptotic expansion methods are not suitable for crystal plasticity simulations at or near fully reversed loading for with the amplitude ratio $R \sim -1$. Large oscillations present in plastic variables during reversible loading conditions lead to dominant higher order terms in the asymptotic series that do not conform to the requirements of monotonically decaying contributions of higher order terms.

This paper proposes a novel wavelet transformation based multi-time scaling (WATMUS) algorithm for accelerated crystal plasticity finite element simulations to overcome the above deficiencies. The wavelet decomposition naturally retains the high frequency response through the wavelet basis functions and transforms the low frequency material response into a “cycle scale” problem undergoing monotonic evolution. No assumption of scale separation is needed with this method. The organization of the paper is as follows. The crystal plasticity constitutive equations in the context of finite element implementation for Ti alloys are discussed in Section 2. A brief review of a few existing methods of time scale acceleration, that assume scale separation, periodicity etc. is given in Section 3. Section 4 introduces the wavelet based multi-time scaling scheme with a brief introduction to wavelets, followed by decomposition into coarse and fine-scale equations with the associated finite element framework. Adaptive methods to improve accuracy and efficiency of the algorithm are discussed in Section 5. Numerical examples for validating the WATMUS algorithm and establishing its capabilities are executed in Section 6. A one dimensional viscoplastic problem is modeled for reverse loading conditions and a 3D crystal plasticity model of a polycrystalline Ti-6Al alloys is simulated under the cyclic loading conditions. The paper is concluded in Section 7 with some concluding remarks.

2. Crystal plasticity constitutive relations

The material that is specifically studied in this work is a polycrystalline titanium alloy Ti-6Al with a hexagonal close packed or *hcp* structure. The *hcp* crystalline structure consists of 5 different families of slip systems as described in [23], including (a) three families of $\langle \mathbf{a} \rangle$ systems, namely 3 equivalent basal $\{0001\} \langle 11\bar{2}0 \rangle$, 3 equivalent prismatic $\{10\bar{1}0\} \langle 11\bar{2}0 \rangle$ and 6 equivalent pyramidal $\{10\bar{1}1\} \langle 11\bar{2}0 \rangle$ systems, and (b) two families of pyramidal $\langle \mathbf{c} + \mathbf{a} \rangle$ systems, namely 12 first order $\{10\bar{1}1\} \langle 11\bar{2}3 \rangle$ and 6 second order $\{11\bar{2}2\} \langle 11\bar{2}3 \rangle$ systems. This constitutes a total of 30 possible slip systems for *hcp* crystals. In Ti alloys, the different slip systems exhibit strong anisotropic behavior both in elasticity and in plasticity. For elasticity, a transversely isotropic response with five independent elastic constants is used [23–25,38]. Plastic deformation occurs by crystallographic slip on the different slip systems. The deformation behavior of the *hcp* material in this paper is modeled using a rate dependent, isothermal, elastic–viscoplastic, finite strain, crystal plasticity formulation following the work [23–25,38]. In this model, crystal deformation results from a combination of the elastic stretching and rotation of the crystal lattice and plastic slip on the

different slip systems. The stress–strain relation is written in terms of the second Piola–Kirchoff stress \mathbf{S} and the work conjugate Lagrange–Green strain tensor \mathbf{E} as

$$\mathbf{S} = \mathbf{C} : \mathbf{E}^e, \quad \text{where } \mathbf{E}^e = \frac{1}{2}(\mathbf{F}^{eT}\mathbf{F}^e - \mathbf{I}) \quad (1)$$

Here \mathbf{C} is a fourth order anisotropic elasticity tensor and \mathbf{F}^e is the elastic component of the deformation gradient which is obtained by multiplicative decomposition

$$\mathbf{F} = \mathbf{F}^e \mathbf{F}^p, \quad \det(\mathbf{F}^e) > 0 \quad (2)$$

where \mathbf{F} is the deformation gradient tensor and \mathbf{F}^p is its plastic component with the incompressibility constraint $\det(\mathbf{F}^p) = 1$. The flow rule governing evolution of plastic deformation is expressed in terms of the plastic velocity gradient as:

$$\dot{\mathbf{L}}^p = \dot{\mathbf{F}}^p \mathbf{F}^{p-1} = \sum_{\alpha}^{\text{nslip}} \dot{\gamma}^{\alpha} \mathbf{s}^{\alpha} \quad (3)$$

where the Schmid tensor associated with α -th slip system \mathbf{s}^{α} is expressed in terms of the slip direction \mathbf{m}_0^{α} and the slip plane normal \mathbf{n}_0^{α} in the reference configuration as $\mathbf{s}^{\alpha} = \mathbf{m}_0^{\alpha} \otimes \mathbf{n}_0^{\alpha}$. For a plastic slip rate $\dot{\gamma}^{\alpha}$ on the slip system α , a power law dependence on the resolved shear stress τ^{α} and the slip system deformation resistance g^{α} has been described in a number of crystal plasticity models [16,18,39] as:

$$\dot{\gamma}^{\alpha} = \dot{\gamma} \left| \frac{\tau^{\alpha} - \chi^{\alpha}}{g^{\alpha}} \right|^{\frac{1}{m}} \text{sign}(\tau^{\alpha} - \chi^{\alpha}), \quad \tau^{\alpha} = (\mathbf{F}^{eT} \mathbf{F}^e \mathbf{S}) : \mathbf{s}^{\alpha} \quad (4)$$

Here m is the material rate sensitivity parameter, $\dot{\gamma}$ is the reference plastic shearing rate and χ^{α} is the back-stress that accounts for kinematic hardening in cyclic deformation.

2.1. Slip system deformation resistance

The evolution of the slip system deformation resistance is assumed to be of the form:

$$\dot{g}^{\alpha} = \sum_{\beta} h^{\alpha\beta} |\dot{\gamma}^{\beta}| \quad (5)$$

The moduli $h^{\alpha\beta} = q^{\alpha\beta} h^{\beta}$ (no sum on β) corresponds to strain hardening rate due to self and latent hardening on the α -th slip system due to slip on the β -th slip system. Here, h^{β} corresponds to the self-hardening and $q^{\alpha\beta}$ is a matrix describing the latent hardening. The evolution of self-hardening, used in [24,25,38], is of the form:

$$h^{\beta} = h_0 \left| 1 - \frac{g^{\beta}}{g_s^{\beta}} \right|^r \text{sign} \left(1 - \frac{g^{\beta}}{g_s^{\beta}} \right), \quad g_s^{\beta} = g_{s0} \left(\left| \frac{\dot{\gamma}^{\beta}}{\dot{\gamma}} \right| \right)^c \quad (6)$$

where h_0 is the initial hardening rate, g_s^{β} is the saturation slip deformation resistance, and r , g_{s0} and c are the slip system hardening parameters.

2.2. Back stress evolution

For modeling cyclic deformation it is important to include kinematic hardening. This has been done by including a backstress in the power law Eq. (4) as in [23,29,40,41]. The resolved effective stress χ^{α} , which is the driving force for the dislocation motion on slip system α is defined as:

$$\dot{\chi}^{\alpha} = c_k \dot{\gamma}^{\alpha} - d_k \chi^{\alpha} |\dot{\gamma}^{\alpha}| \quad (7)$$

In Eq. (7), c_k and d_k are the direct hardening and dynamic recovery coefficients, respectively.

2.3. Size effect

Experimental studies on alloy systems have shown the dependence of flow stress on grain size due to grain boundary strengthening with saturation at a threshold value of grain size. To account for size effects in crystal plasticity formulation, a Hall–Petch type relationship that relates the slip system deformation resistance to a characteristic length scale has been incorporated [26,27]. The dependence is expressed as:

$$g^{\alpha} = g_0^{\alpha} + \frac{K^{\alpha}}{\sqrt{D^{\alpha}}} \quad (8)$$

where g_0^{α} and K^{α} are size effect related slip system constants that refer to the interior slip system deformation resistance and slope respectively, and D^{α} is the characteristic length scale governing the size effect (such as the grain size).

The calibrated elastic and crystal plasticity material constants are listed in Tables 1 and 2 respectively.

3. Review of some accelerated time integration methods for cyclic plasticity

Simulating a large number of cycles for crystal plasticity simulations is computationally prohibitive using conventional FEM with a single time scale integration. In these conventional methods of numerical time integration using semi-discretization, each cycle is discretized into a number of time steps for time integration. A high time step resolution may be required for each cycle, depending on the evolution pattern of the response variables throughout the loading process. In addition, it is often necessary to conduct simulations for a significantly high number of cycles to reach local states of damage initiation and growth. This presents a significant challenge due to the presence of two distinct time scales, viz.:

1. The fine time scale τ of each cycle, dictated by the frequency of loading
2. The coarse time scale t of material evolution, characterized by the material relaxation time or time to failure.

To overcome this challenge, a variety of accelerated time integration methodologies have been devised in the literature. The following subsections discuss the feasibility and shortcomings of these approaches in reference to the rate dependent plasticity problem that is being solved here.

3.1. Extrapolation based methods

In extrapolation methods, the cyclic response of a representative microstructural volume is simulated up to a certain number of cycles and the evolution of state variables are extrapolated from these results thereafter. High cycle fatigue problems have been studied in [12], where fatigue cracks usually initiate after thousands of cycles. However, only two complete strain cycles were simulated to obtain fatigue parameters with the assumption that the response stabilizes thereafter. Fretting fatigue in titanium alloys has been studied using a cyclic crystal plasticity model in [42,43], where the response is assumed to stabilize after three load cycles. An extrapolation based approach has also been utilized in [30] for predicting fatigue life of HSLA steels from the results

Table 1
Transverse isotropic elastic stiffness parameters for Ti-6AL.

Elastic stiffness components (GPa)	C_{11}	C_{12}	C_{13}	C_{33}	C_{55}
	170	98	86	204	51

Table 2
Crystal plasticity parameters in the hcp model for Ti-6AL.

CP Parameters	Basal	Prismatic	Pyramidal <a>	Pyramidal
	<a> slip	<a> slip	<a> slip	<c + a> slip
$\dot{\gamma}_0$	0.0023	0.0023	0.0023	0.0023
m	0.02	0.02	0.02	0.02
g_0 (MPa)	284	282.24	395	623.3
K (MPa $\sqrt{\mu\text{m}}$)	164.5	164.5	164.5	164.5
h_0 (MPa)	100	100	100	100
r	0.1	0.1	0.1	0.1
n	0.01	0.01	0.01	0.01
g_s (MPa)	450	550	550	1650

of crystal plasticity simulations. The stabilized plastic strain response is used to derive a functional relationship for the local ratcheting rate in terms of the number of cycles and the mean applied stress, of the form:

$$\frac{d\varepsilon^p}{dN} = \left[\frac{d\varepsilon^p}{dN} \right]_1 - C_1 \left(1 - \frac{1}{N(1 + \ln(N))^{C_2}} \right) \quad (9)$$

where C_1 and C_2 are parameters which depend on the applied mean stress and $\left[\frac{d\varepsilon^p}{dN} \right]_1$ is the ratcheting rate for the first cycle.

A major drawback of the extrapolation based approaches is that they fail to adequately track the evolution of microstructural variables that are often highly localized, e.g. the phenomenon of load shedding from one grain to its neighbors. This can lead to significant errors in the predicted value of the microstructural state variables and can render any microstructure based crack initiation criterion completely inaccurate. Another issue with these methods is that their accuracy is very sensitive to the point or points in time, from which values are being extrapolated. Reaching a stabilized state at all points in the polycrystalline microstructure may involve simulating a considerable number of cycles before the extrapolation is carried out. Even then, it does not exclude the possibility of inaccurate representation of local deformation states in the microstructure that are crucial for predicting fatigue life.

As a test of the extrapolation algorithms, a one-dimensional viscoplastic bar problem is solved with the following constitutive relations and boundary conditions.

$$\sigma = E(\varepsilon - \varepsilon^p), \quad \dot{\varepsilon}^p = \dot{g} \left| \frac{\sigma}{g} \right|^m \text{sign}(\sigma) \quad \dot{g} = h |\dot{\varepsilon}^p| \quad (10)$$

$$\text{with } \varepsilon^p(x, t = 0) = 0 \text{ and } g(x, t = 0) = \begin{cases} g_{o1} & \text{for } 0 < x < L \\ g_{o2} & \text{for } L < x < 2L \end{cases}$$

with $\sigma, \varepsilon, \varepsilon^p, g, m$ and a being the stress, strain, plastic strain, hardness, rate sensitivity exponent and reference strain rate. The cyclic boundary conditions imposed are:

$$u(x = 0, t) = 0 \text{ and} \quad (11)$$

$$u(x = 2L, t) = \bar{u}_0 + \tilde{u}_0 \sin\left(\frac{2\pi t}{\zeta}\right) \text{ with } \zeta \rightarrow 0$$

Eqs. (10) and (11) are solved using the finite element method using two 1-D bar elements for up to 2000 cycles of the applied displacement loading. Material parameters used are shown in Table 3 and the time period of the applied loading is 1 s i.e. $\zeta\tau_0 = 1$.

For testing the extrapolation based schemes, the simulation is continued till stabilization in plastic strain occurs corresponding to $\Delta\varepsilon^p(N) \leq 10^{-3} \times \varepsilon^{p0}(N)$. Here $\varepsilon^{p0}(N)$ is the plastic strain at the beginning of cycle N and $\Delta\varepsilon^p(N)$ is the change in plastic strain over the N -th cycle. For the problem considered, stabilization occurs at around

Table 3
Properties for the 1-D visco-plastic problem.

E (MPa)	\dot{a} (s $^{-1}$)	m	g_{o1} (MPa)	g_{o2} (MPa)	h (MPa)
200×10^3	0.0023	0.02	320	600	100

$N_o = 1590$ cycles and the variable $\varepsilon^{p0}(N)$ is extrapolated from the corresponding state using the formula:

$$\varepsilon^{p0}(N) = \varepsilon^{p0}(N_o) + \left(\varepsilon^{p0}(N_o + 1) - \varepsilon^{p0}(N_o) \right) (N - N_o) \quad N > N_o \quad (12)$$

Fig. 1 shows a comparison of the extrapolated solution with the completely solved finite element solution for 2000 cycles. The extrapolated solution accumulates error with increasing cycles, with an error of approximately 12% at around 5000 cycles even in this macroscopic variable. In another scheme, a cubic polynomial is fitted with the initial values of the plastic strain and the corresponding extrapolation is shown. This also fails in capturing the response after the stabilized cycle. It is obvious that these methods are likely to produce significant local errors even when overall stabilization has been achieved in the solution.

3.2. Block integration methods

Block integration methods divide the entire loading history into a series of blocks and subsequently evaluate the evolution of state variables within a block by using their starting values within the block. Block integration schemes have been developed in the context of continuum damage mechanics in [44–46]. In these methods a constant amplitude loading history is subdivided into a series of load cycle blocks. Each block consists of a series of load reversals between two fixed amplitudes. As pointed out in [46], limitations of these approaches are as follows:

- Solutions deviate from the equilibrium path caused by assumptions in the integration of the fatigue damage accumulation law (damage evolution independent of stress).
- It is difficult to estimate the adequate block size especially when the growth of the fatigue damage is high.
- The methods have limited applicability to heterogeneous materials.

As a remedy, the cyclic derivative of the damage parameter using an incremental finite element analysis has been proposed in [46]. This is

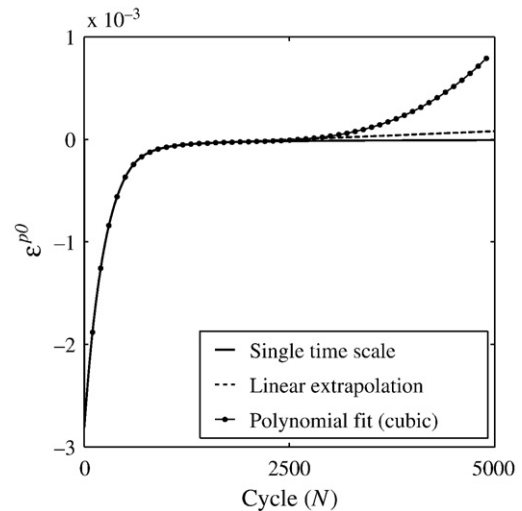


Fig. 1. Comparison between the single scale and extrapolated solution for the 1-D problem.

then integrated over multiple cycles by a modified Euler approach with time step control. However, this approach violates the constitutive relations due to keeping state variables fixed while updating the damage variables, and a consistency adjustment procedure is required. Consequently, the number of cycles traversed in each step can turn out to be very small and the method will lose its advantage. Additionally, the consistency adjustment procedure can lead to non-uniqueness in the solution.

3.3. Dual time scale methods

Limitations of the previous approaches have led to the development of dual time scale methods [36,37,47] that assume the existence of two time scales in the solution to the governing equations. The first corresponds to a coarse time scale t that characterizes the slow varying behavior of the solution, while the second is a fine time scale τ that characterizes the fast varying behavior. The methods rely on decoupling the problem into a set of coarse scale and fine scale evolution equations. Typically, a one-way coarse to fine scale coupling is necessary for harnessing the full computational advantage of these methods. The high frequency component is either approximated or is calculated explicitly and is used in a set of integro-differential equations for the low frequency response. The coarse scale equations, describing the low frequency behavior, can be integrated with significantly larger time steps compared to the normal cycle by cycle integration method. The fine scale evolution equations, corresponding to the high frequency component of the solution, are used to reconstruct the full solution at any point in the coarse time scale. Two approaches in this category are discussed next for their suitability to this class of problems.

3.3.1. Asymptotic expansion based methods

Dual time scale methods, proposed in [36,37,47] make use of an asymptotic expansion of the primary state variables to decouple their coarse and fine scale evolution. Yu and Fish [36] have proposed a temporal homogenization method in which they assumed all the variables to be locally periodic in time. This assumption was nominally relaxed in [47] to include variables, which are nearly periodic in time. Temporal periodicity or even near-periodicity are however not valid assumptions for evolving microstructural variables in crystal plasticity simulations under certain loading conditions. In addition, these methods may invoke two-way coupling between the time scales that requires solution of initial value problems at both time scales in each step. This can result in very high computational cost and may not provide any advantage over single time scale calculations.

To avoid two-way coupling, Ghosh et al. [37,48] have developed a decoupled set of crystal plasticity based governing equations. The problems are characterized by a cycle-averaged, low frequency behavior and a short time scale (high frequency) problem for the remaining oscillatory portion. Effective constitutive equations are developed for the cycle-averaged problem by interpolating in a parameter space that is created from single time scale solutions of single slip-system problems. The resulting averaged constitutive equations do not assume periodicity and are decoupled from the short time scale oscillatory behavior. Consequently, they can be solved with time increments that are of the order of multiple time periods of the cyclic loading. This can yield significant computational gain over single time scale solution. Furthermore, asymptotic expansions of various field variables are used to decompose the oscillatory problem into various orders of oscillations. Each order of oscillatory solution can be solved locally in temporal domain with the knowledge of the averaged solution. While computational efficiency can be significantly enhanced with this method for certain problems, the asymptotic expansion based methods can face serious deficiencies for some load cases as discussed later in this section.

The main idea of the asymptotic methods and its application in [37,48] can be understood through the 1-D viscoplastic problem introduced in Section 3.1. All state variables, e.g. plastic strain, stress

and hardness at a point x are assumed to depend on the two scales t and τ and may be expressed in terms of an asymptotic series as:

$$\varepsilon^{p(\zeta)}(x, t, \tau) = \varepsilon^{p(0)}(x, t, \tau) + \zeta \varepsilon^{p(1)}(x, t, \tau) + \mathcal{O}(\zeta^2) \quad (13)$$

$$\sigma^\zeta(x, t, \tau) = \sigma^{(0)}(x, t, \tau) + \zeta \sigma^{(1)}(x, t, \tau) + \mathcal{O}(\zeta^2)$$

$$g^\zeta(x, t, \tau) = g^{(0)}(x, t, \tau) + \zeta g^{(1)}(x, t, \tau) + \mathcal{O}(\zeta^2)$$

In addition, these evolving variables $\phi(x, t, \tau)$ can be decomposed into their average and oscillator parts as:

$$\bar{\phi}(x, t) = \frac{1}{\tau_0} \int_{\frac{t}{\tau_0}}^{\frac{t}{\tau_0} + \tau_0} \phi(x, t, \tau) d\tau = \langle \phi \rangle \quad \phi_{osc}(x, t, \tau) = \phi(x, t, \tau) - \bar{\phi}(x, t) \quad (14)$$

Substituting these decompositions into the constitutive equations and separating terms corresponding to various orders of $\varepsilon^{p(\zeta)}$ result in:

$$\mathcal{O}(\zeta^{-1}) : \quad \frac{\partial \varepsilon_{osc}^{p(0)}}{\partial \tau} = 0 \Rightarrow \varepsilon^{p(0)}(t, \tau) = \bar{\varepsilon}^{p(0)}(t) \quad \text{and} \quad \varepsilon_{osc}^{p(0)}(t, \tau) = 0 \quad (15a)$$

$$\frac{\partial g_{osc}^{(0)}}{\partial \tau} = h \text{sign}(\sigma) \frac{\partial \varepsilon_{osc}^{p(0)}}{\partial \tau} = 0 \quad (15b)$$

$$\mathcal{O}(\zeta^0) : \quad \frac{\partial \varepsilon^{p(0)}}{\partial t} + \frac{\partial \varepsilon^{p(1)}}{\partial \tau} = \dot{a} \left| \frac{\sigma^{(0)}}{g^{(0)}} \right|^m \text{sign}(\sigma) \quad (15c)$$

$$\frac{\partial g_{osc}^{(0)}}{\partial t} + \frac{\partial g^{(1)}}{\partial \tau} = h \text{sign}(\sigma) \left(\frac{\partial \varepsilon^{p(0)}}{\partial t} + \frac{\partial \varepsilon^{p(1)}}{\partial \tau} \right) \quad (15d)$$

Local temporal periodicity, that has been assumed in [36,47], is in general not valid for problems involving plastic accumulation due to evolving hardness and other parameters. From the asymptotic analysis, the plastic strain oscillator is derived to be of $\mathcal{O}(\zeta)$. This implies that the stress oscillator σ_{osc}^ζ is of the form:

$$\sigma_{osc}^\zeta = E \varepsilon_{osc} - \zeta E \varepsilon_{osc}^{p(1)} + \mathcal{O}(\zeta^2) \quad (16)$$

Considering only $\mathcal{O}(\zeta^0)$ contributions, the stress oscillator can be assumed to be elastic i.e. $\sigma_{osc}^\zeta \approx E \varepsilon_{osc}$ as long as $\zeta \varepsilon^{p(1)} \rightarrow 0$. This result ensures that the stress oscillator can be obtained at every material point by simulating a single cycle. The approach used in [37,48] makes use of this property and assumes a coarse scale evolution equation for the average plastic strain of the form:

$$\frac{d \bar{\varepsilon}^p}{dt} = f \left(\bar{\sigma}, \sigma_{osc}^{char}, \bar{g} \right) \quad (17)$$

thereby decoupling the average and the oscillatory parts of the problem. The function f is obtained through a calibration process. In Eq. (17), σ_{osc}^{char} is selected as a characteristic function of the stress oscillator, e.g. the stress amplitude. From the results of the asymptotic analysis, the stress oscillator may be assumed to remain constant at a material point from cycle to cycle. Eq. (17) can now be used to integrate over many cycles in one integration step over coarse time t .

Remark 1. Failure of the asymptotic methods for certain R ratios.

Load reversal in cyclic loading is expressed in terms of the R ratio, defined as $R = \frac{\sigma_{min}}{\sigma_{max}}$. While the asymptotic expansion based methods work well for loads that are not in the vicinity of fully reversed loading i.e. for $R \neq -1$, they face severe limitations as the loads approach the

fully reversed loading case i.e. $R \rightarrow -1$. Large oscillations in the plastic variables are encountered near $R = -1$ that violate the assumption of decay of higher order terms in the asymptotic expansion. This implies that the stress oscillator is no longer elastic and has a strong inelastic component. Hence it is not possible to characterize it at a point across multiple cycles from the results of just one cycle. As a result, equations of the form (17) are not usable in such situations as discussed next.

The 1-D bar is subjected to an applied harmonic strain of $\varepsilon(t, \tau) = \bar{\varepsilon}_0 + \tilde{\varepsilon}_0 \sin\left(\frac{2\pi\tau}{T_0}\right)$. Here t represents the coarse or slow varying time scale and $\tau = \frac{t}{\zeta}$ with $\zeta \rightarrow 0$ represents the fast varying time scale. Application of chain rule together with a relation connecting derivatives in the two scales results in:

$$\frac{\partial \varepsilon^{p(\zeta)}}{\partial t} + \frac{1}{\zeta} \frac{\partial \varepsilon^{p(\zeta)}}{\partial \tau} = \dot{a} \left| \frac{E\left(\bar{\varepsilon}_0 + \tilde{\varepsilon}_0 \sin\left(\frac{2\pi\tau}{T_0}\right) - \varepsilon^p\right)}{g} \right|^{\frac{1}{m}} \text{sign}(\sigma) \quad (18)$$

Using the asymptotic expansion in Eq. (13) for a simplified case with $m = 1$ and $h = 0$, the following solution can be obtained analytically:

$$\begin{aligned} \varepsilon^{p\zeta} &= \bar{\varepsilon}^{p(0)}(t) + \zeta(\bar{\varepsilon}^{p(1)}(t) + \varepsilon_{osc}^{p(1)}(t, \tau)) + \mathcal{O}(\zeta^2) \dots, \text{ with} \\ \bar{\varepsilon}^{p(0)}(t) &= \bar{\varepsilon}_0 \left(1 - e^{-\frac{t}{t_r}}\right), \quad \bar{\varepsilon}^{p(1)}(0) = \frac{T_0}{2\pi t_r}, \quad \varepsilon_{osc}^{p(1)} = -\tilde{\varepsilon}_0 \frac{T_0}{2\pi t_r} \cos\left(\frac{2\pi\tau}{T_0}\right) \end{aligned} \quad (19)$$

Additionally the stress expansion is

$$\begin{aligned} \sigma^\zeta(t, \tau) &= \bar{\sigma}^\zeta(t) + \sigma_{osc}^\zeta(t, \tau), \text{ where} \\ \bar{\sigma}^\zeta &= E\left(\bar{\varepsilon}_0 - \bar{\varepsilon}^{p(0)}\right) - \zeta E \bar{\varepsilon}^{p(1)} + \mathcal{O}(\zeta^2), \text{ and} \\ \sigma_{osc}^\zeta(t, \tau) &= E \tilde{\varepsilon}_0 \sin\left(\frac{2\pi\tau}{T_0}\right) + \zeta E \varepsilon_{osc}^{p(1)} + \mathcal{O}(\zeta^2) \end{aligned} \quad (20)$$

with $t_r = \frac{g}{\dot{a}E}$. This solution demonstrates that as long as $\zeta \varepsilon_{osc}^{p(1)} \rightarrow 0$, the stress oscillator is elastic and can be obtained from just one cycle of the simulation. This is a key assumption in [36,37] and it is true as long the first order plastic strain $\varepsilon_{osc}^{p(1)}$ remains relatively small i.e. the oscillations in the plastic strain are not excessive. For an applied reversible sinusoidal loading with amplitude 0.006 and time period of 1 s, the variation of different orders of the stress oscillator over one cycle is shown in Fig. 2.

The figure shows that the first order stress oscillator contribution is around 22% of the elastic stress oscillator. Consequently, it cannot be

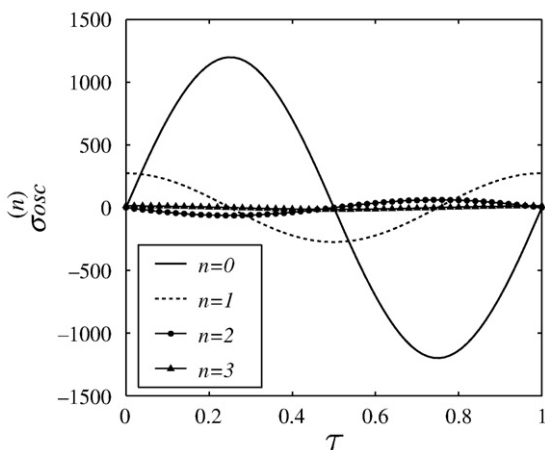


Fig. 2. Various orders of the stress oscillator in the asymptotic expansion ($n = 0$ is the elastic stress oscillator).

neglected in the construction of the stress. From Eq. (19), the amplitude of the first order plastic strain oscillator is proportional to $\tilde{\varepsilon}_0$ i.e. the oscillatory part of the applied strain. Using the first order terms in σ^ζ to calculate the R ratio, the following relationship is obtained:

$$\tilde{\varepsilon}_0 \approx \begin{cases} \frac{1}{2} \{1-R\} (|\bar{\varepsilon}_0| + |\tilde{\varepsilon}|_{\max}) & \text{for } |R| \leq 1 \\ \frac{1}{2} \left\{1 - \frac{1}{R}\right\} (|\bar{\varepsilon}_0| + |\tilde{\varepsilon}|_{\max}) & \text{for } |R| \geq 1 \end{cases} \quad (21)$$

The normalized amplitude of the plastic oscillator, denoted as (normalized $|\varepsilon_{osc}^{p(1)}|_{\max} = \frac{2\pi t_r}{|\bar{\varepsilon}_0| + |\tilde{\varepsilon}|_{\max}} |\varepsilon_{osc}^{p(1)}|_{\max}$) is plotted as a function of R in Fig. 3. Here t_r is a material parameter and $|\bar{\varepsilon}_0| + |\tilde{\varepsilon}|_{\max}$ is the maximum absolute value of the applied strain. The maximum value of the plastic strain oscillator $\varepsilon_{osc}^{p(1)}$ occurs as $R \rightarrow -1$. Therefore the possibility of large oscillations in the plastic strain increases as $R \rightarrow -1$ and hence the stress oscillator does not remain elastic.

The same inference is made for the case of $m = 0.02$ in Fig. 4, where again the stress oscillator does not remain constant with progressing cycles. In addition to changes in the magnitude, there is a change in the shape of the oscillator waveform as well. This makes it difficult to obtain a characteristic value (σ_{osc}^{char}) to be used in Eq. (17).

The above study on the use of asymptotic expansion based methods for multi-time scaling of rate dependent plasticity equations is helpful for making the following conclusions.

1. Asymptotic expansion of state variables in the viscoplastic constitutive laws results in the condition that the plastic oscillations are of $\mathcal{O}(\zeta)$ or are very small.
2. As a consequence of the negligible plastic oscillations, the stress oscillator remains elastic and therefore shows very little variation across cycles. The decoupling between the scales is then achieved by integrating only the slow varying or low frequency components like the average response with large time increments. On the other hand, the fast varying or high frequency components remain the same across the cycles (stress oscillator) or are negligible (plastic strain oscillations).
3. In the case of reversible loading, the plastic oscillations are not negligible and the assumption of asymptotic decay of the successive terms in the series does not hold. The stress oscillator is now inelastic and needs to be explicitly solved from cycle to cycle. As a result, the decoupling that was possible earlier is no longer accurate, as the high frequency components have to be explicitly accounted for with progressing cycles.

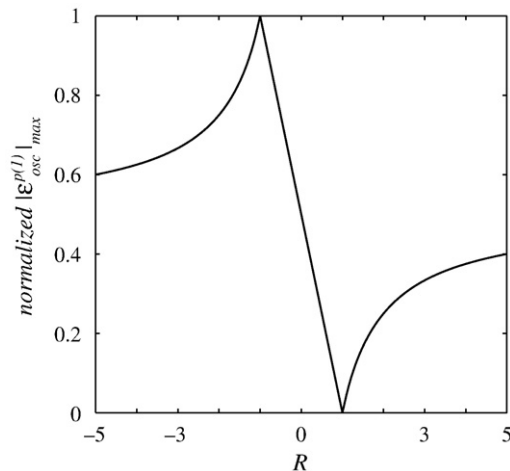


Fig. 3. Effect of R ratio on the amplitude of plastic oscillator using a normalizing factor $\frac{2\pi t_r}{|\bar{\varepsilon}_0| + |\tilde{\varepsilon}|_{\max}}$.

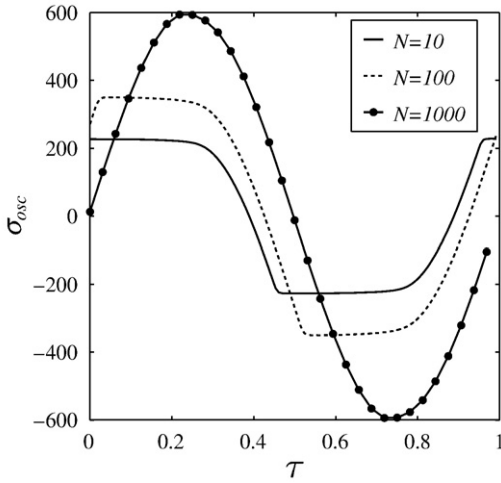


Fig. 4. Comparison of the stress oscillator across different cycles for $R = -1$.

3.3.2. Methods on homogenization of almost periodic functions

Oskay and Fish [35] have proposed an a-periodic temporal homogenization (APTH) operator to track the evolution of almost-periodic variables. Such near-periodicity may arise in constitutive laws due to irreversibility or damage accumulation. The averaging APTH operator $\langle \cdot \rangle_{APTH}$ acting on the a-periodic function $\phi_{ap}(x, t, \tau)$ has been defined in [35] through a coarse scale differential equation as:

$$\frac{d\langle \phi_{ap}^\xi \rangle_{APTH}}{dt} = \langle \dot{\phi}_{ap}^\xi \rangle(t) \tag{22}$$

The fine time scale response of the function denoted by $\tilde{\phi}_{ap}^\xi$ is defined as:

$$\tilde{\phi}_{ap} = \phi_{ap}(t, \tau) - \langle \phi_{ap} \rangle_{APTH}(t) \tag{23}$$

The 1-D viscoplastic model of Section 3.1 can be resolved into a coupled set of coarse and fine time scale initial-boundary value problems by using the APTH operator. The equations are solved using a staggered, global–local, integration scheme. In this adaptive scheme, coarse scale variables $\langle \phi \rangle_{APTH}(t_{n+1})$ at time t_{n+1} are updated, while keeping the fine scale variables at t_n i.e. $\tilde{\phi}_{n+1} = \tilde{\phi}_n$. The local, fine scale initial-boundary value problem is then solved with the updated values of the coarse variables over the time domain $[0, \tau]$.

This global–local method does not make use of the asymptotic expansion and hence does not suffer from the limitations pertaining to $R \rightarrow -1$. However if the coupling between the two scales is strong, it may lead to very small time steps in the coarse scale, thus affecting the computational efficiency adversely. This is illustrated for the 1-D viscoplastic problem in Fig. 5 for the fully reversible loading case $R = -1$. The results show increasing instability with higher step sizes (number of cycles traversed in each step) in the staggered approach. Fig. 5 shows oscillations in the solution for step size of two cycles, i.e. $\Delta N = 2$, while for $\Delta N = 4$ it leads to complete instability. The method does give accurate result for $\Delta N = 1$, but this corresponds to the normal cycle by cycle or fine scale integration with no computational advantage. In summary, the global–local approach using the APTH operator suffers from the following limitations for simulating rate dependent crystal plasticity problems.

1. The inability to solve the entire set of governing equations (equilibrium and constitutive) in a consistent manner leads to global–local or staggered approach, where one set of fields are artificially kept constant while the others are updated.
2. This approach may require unreasonably small time steps to preserve stability in the crystal plasticity simulations, thus negating the proposed time advantage due to decoupling.

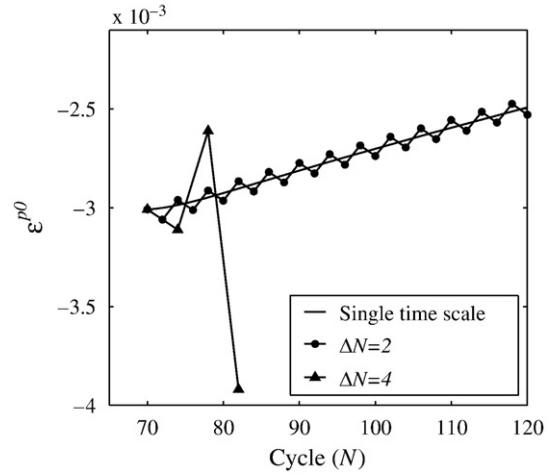


Fig. 5. Comparison of the fine-scale solution with the APTH operator based solution with different step sizes, for the 1-D viscoplastic problem.

In this paper, a new wavelet transformation based multi-time scaling method is introduced as a promising alternative to all the time acceleration methods discussed in this section. Unlike some of the conventional approaches, this method makes no assumption on the periodicity of the solution or asymptotic behavior of variables. The method is valid under all conditions of loading including the fully reversible case.

4. Wavelet transformation based multi-time scaling methodology for cyclic crystal plasticity simulations

The wavelet transformation based multi-time scaling (WATMUS) methodology for accelerated time integration in crystal plasticity finite element analyses may be motivated by the viscoplastic response of a material undergoing cyclic plastic deformation. Shown in Fig. 6(a) is the evolution of a rate dependent crystal plasticity state variable (y), solved by the finite element method. Clearly, the material response can be resolved into two time scales, viz. (i) a rapidly oscillating response within each cycle corresponding to a fine time scale τ as shown in Fig. 6(b,c), and (ii) a slowly varying monotonic response over the entire loading time span as shown in Fig. 6(d), corresponding to a coarse time scale t . The coarse time scale in this methodology can be identified with the cycle scale N , and hence projects a monotonic behavior. Correspondingly, the value of any given state variable y_o at the beginning of a given cycle can be thought of as a coarse time scale variable. This state variable will not vary in the τ -scale within each cycle and hence, it can be considered to be purely a function of the cycle number N , i.e. $y^o = y^o(N)$. The objective then is to obtain a coarse time scale (cycle scale) evolution equation of the form:

$$\frac{dy^o}{dN} = f(y^o(N), \epsilon^k(N)) \tag{24}$$

where $\epsilon^k(N)$ are the wavelet decomposed strain coefficients over the cycle N that is resolved with respect to wavelet basis functions $\psi_k(\tau)$ in the τ -scale. Note that without the wavelet components $\epsilon^k(N)$, it is not possible to obtain the right hand side in Eq. (24) and a global–local approach would have to be used along with its limitations. Thus, any variable, e.g. the strain can be resolved in a wavelet basis as:

$$\epsilon(x, t) = \epsilon(x, N, \tau) = \sum_k \epsilon^k(x, N) \psi_k(\tau) \tag{25}$$

The coefficients $\epsilon^k(x, N)$ depends only on the cycle number N and the location x in the material microstructure. It is important to note that the τ -scale basis functions $\psi_k(\tau)$ do not change with cycles N . For any material variable, the coarse scale behavior is associated with the cycle number N and the fine scale behavior with the time scale $\tau \in [0, T]$,

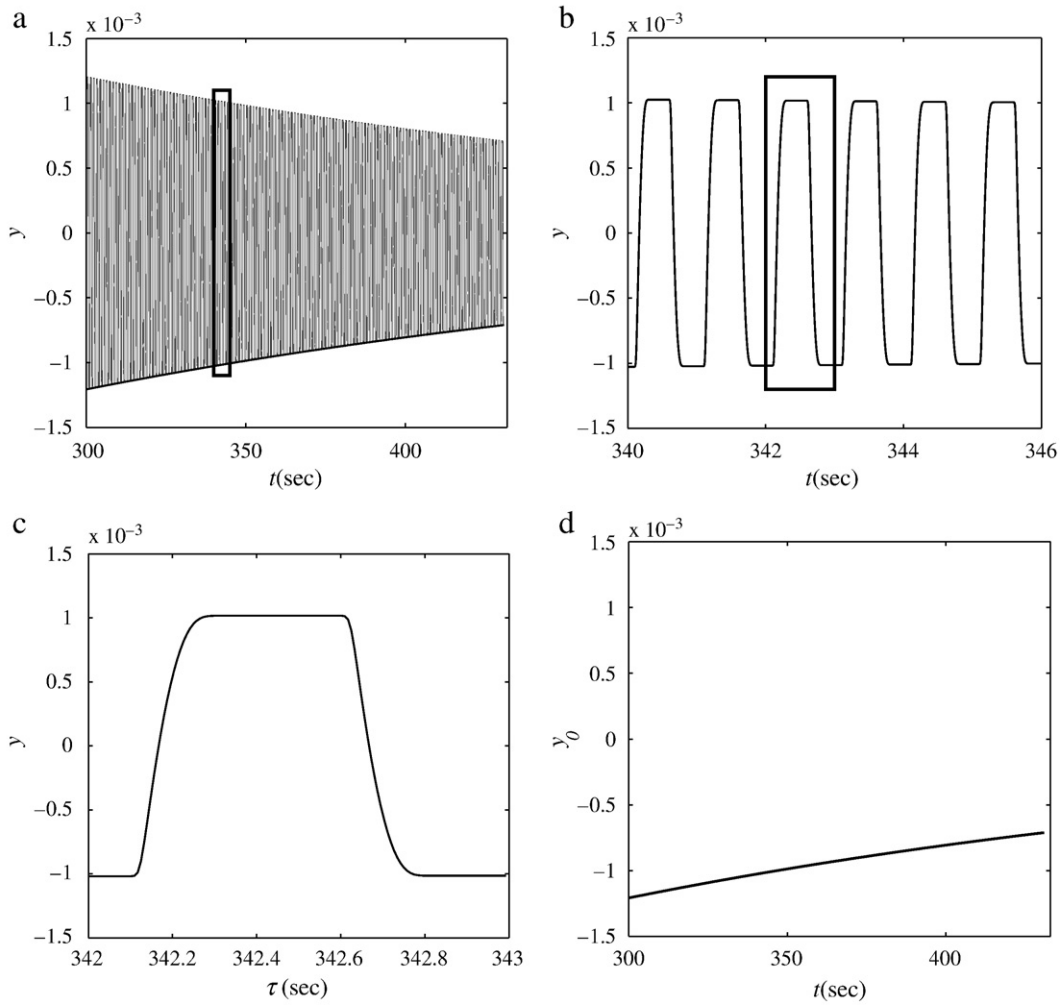


Fig. 6. Decoupling the fine and coarse time scale responses for a chosen viscoplastic state variable under cyclic loading: (a) fine scale solution, (b,c) zoomed in fine scale solution, (d) coarse scale solution corresponding to the value at the start of a cycle.

T being the loading period. Equations (24) and (25) can then be used to delineate the coarse and fine scale behavior of the constitutive equations. A single integration step of Eq. (24) can traverse many cycles ΔN , resulting in significant computational efficiency of the algorithm. The value of ΔN is expected to increase with response stabilization.

The WATMUS methodology introduced in this work requires appropriate basis functions for temporally resolving the displacement vector, and the corresponding strain or deformation gradient fields as in Eq. (25). An ideally chosen set of basis functions should satisfy the following conditions:

- The functions should be orthogonal, i.e. form a linearly independent set.
- The functions should be able to represent all possible waveforms in the response variables to a pre-determined resolution.
- The number of coefficients, corresponding to the number of basis functions used in this representation must be optimally small. This should hold even as the number evolves with progressing cyclic deformation.

A spectral basis representation in terms of Fourier series functions suffer from the following shortcomings:

- The basis functions in a Fourier series have infinite support. The use of a finite set of Fourier coefficients, while truncating others in the infinite series, can lead to instabilities in the oscillatory response. Such instabilities, e.g. the Gibbs phenomenon give spurious oscillations at regions where the signal is cut-off. This in turn can lead to inaccuracies in the coarse scale solution.

- The dominant terms, needed to match a response signal, are not known a-priori in the selection of a finite subset of the infinite Fourier series. A trial and error process is needed to establish these terms.

It is deemed that a basis of wavelet functions avoids these shortcomings and hence is considered for the multi-time scale (WATMUS) approach developed here.

4.1. Brief overview of wavelet basis functions

Wavelet basis functions span the space of square integrable functions $L^2(R)$ through translation and dilation of the scaling function $\phi(\tau)$ [49,50], which satisfies the following refinement condition:

$$\phi(\tau) = \sum_{k=1}^{N_{fit}} h_k \phi(2\tau - k) \quad (26)$$

Parameters h_k and N_{fit} characterize the wavelet basis and correspond to the components of a low pass filter. Any function in this space can be expressed as:

$$f(\tau) = \sum_m \sum_n C_{m,n} \phi_{m,n}(\tau) \quad (27)$$

where $\phi_{m,n} = 2^{\frac{m}{2}} \phi(2^m \tau - n)$ with $m, n \in \mathbb{Z}$ corresponding to the dilation and translation of ϕ respectively. This means that at a

certain resolution, the subspace is spanned by translations of the scaling function in Eq. (26), dilated to that resolution. The scaling function $\phi(\tau)$ function may be used to produce a multiresolution analysis in $L^2(R)$ using the property:

$$\{0\} \subset \dots \subset V_{-1} \subset V_0 \subset V_1 \subset \dots \subset V_m \subset V_{m+1} \subset \dots \subset L^2(R) \tag{28}$$

where V_m denotes the subspace of $L^2(R)$ at resolution m with the basis ϕ_{mn} . A complimentary space of interest in the multiresolution analysis is the detail space W_m , which contains the orthogonal difference between two consecutive resolutions V_m and V_{m+1} i.e. $V_{m+1} = V_m \oplus W_m$. The basis functions for this space is generated in a similar manner to that of V_m , through the translation and dilation of a mother wavelet function $\psi(\tau)$, i.e. $W_m = span\{\psi_{m,n} = 2^m \psi(2^m \tau - n), m, n \in Z\}$. The mother wavelet satisfies a condition similar to Eq. (26):

$$\psi(\tau) = \sum_{k=1}^{N_{fit}} g_k \phi(2\tau - k) \tag{29}$$

where g_k corresponds to the components of a high pass filter and is another characteristic of the wavelet basis. In other words the wavelet basis can be completely represented through the filter coefficients h_k and g_k using Eqs. (26) and (29). Filter coefficients for the Daubechies-4 wavelet used in the present work (see [51]) are given as:

$$\begin{aligned} h_1 &= \frac{1 + \sqrt{3}}{4}, h_2 = \frac{3 + \sqrt{3}}{4}, h_3 = \frac{3 - \sqrt{3}}{4}, h_4 = \frac{1 - \sqrt{3}}{4} \\ g_1 &= \frac{1 - \sqrt{3}}{4}, g_2 = \frac{-3 + \sqrt{3}}{4}, g_3 = \frac{3 + \sqrt{3}}{4}, g_4 = \frac{-1 - \sqrt{3}}{4} \end{aligned} \tag{30}$$

These coefficients are obtained from the following considerations:

- Compact support: The Daubechies-4 wavelet has four filter coefficients ($N_{fit}=4$). This leads to a $\phi(\tau)$ and $\psi(\tau)$ with support [0,3]
- Orthogonality of translation: Scaling functions obtained through the coefficients h_k satisfy $\int_{-\infty}^{\infty} \phi(\tau - k)\phi(\tau - l)d\tau = \delta_{kl}$.
- Smoothness: Coefficients are selected so as to have the maximum number of vanishing moments for a given support (2 in the case of Daubechies-4 wavelet). This implies that the basis can capture a linear function exactly.

Using Eq. (26) at discrete points $\tau=0,1,2,3$ in the time scale and setting to zero the points outside the compact support [0,3] results in the following equation:

$$\begin{Bmatrix} \phi(0) \\ \phi(1) \\ \phi(2) \\ \phi(3) \end{Bmatrix} = \begin{bmatrix} h_1 & 0 & 0 & 0 \\ h_3 & h_2 & h_1 & 0 \\ 0 & h_4 & h_3 & h_2 \\ 0 & 0 & 0 & h_4 \end{bmatrix} \begin{Bmatrix} \phi(0) \\ \phi(1) \\ \phi(2) \\ \phi(3) \end{Bmatrix} \tag{31}$$

One of the eigen-values of the square matrix on the right hand side of the above equation may be set to 1, through appropriate choice of h_k in Eq. (30). Correspondingly, the values of the scaling function at $\tau=0,1,2,3$ are obtained from the eigen-vector and this is used as starting values in the following recursive relationship once again obtained from Eq. (26):

$$\begin{aligned} \phi\left(\frac{n}{2^j}\right) &= h_1 \phi\left(\frac{n}{2^{j-1}}\right) + h_2 \phi\left(\frac{n}{2^{j-1}} - 1\right) + h_3 \phi\left(\frac{n}{2^{j-1}} - 2\right) + h_4 \phi\left(\frac{n}{2^{j-1}} - 3\right) \\ \forall n &= 1, 2, \dots, 3 \cdot 2^j, j = 1, 2, 3, \dots \end{aligned} \tag{32}$$

A similar procedure can be obtained for the mother wavelet $\psi(\tau)$. The values so obtained for the scaling function and the mother wavelet are shown in Fig. 7.

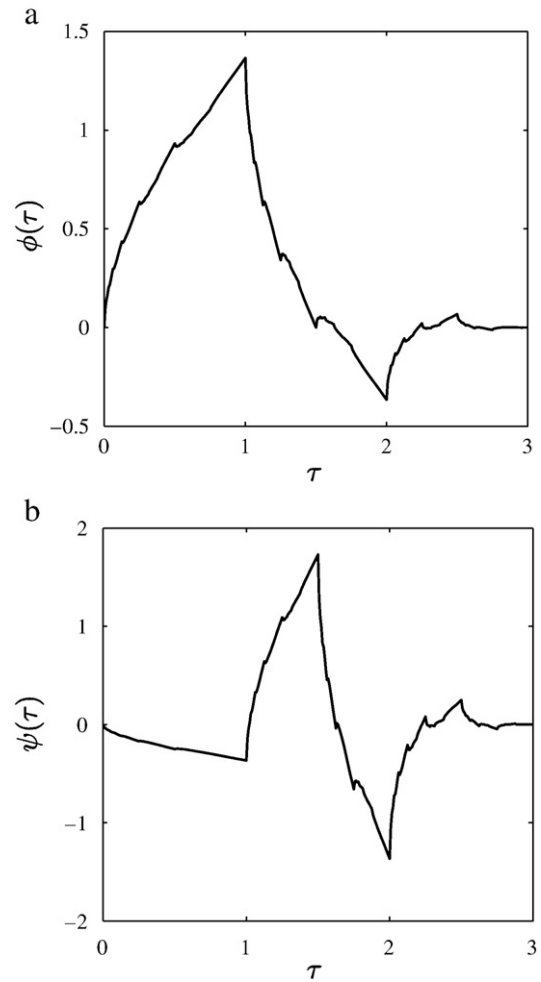


Fig. 7. Daubechies-4 wavelets: (a) Scaling function ϕ , and (b) Mother wavelet ψ .

A function, belonging to the space V_m , can thus be split into two orthogonal components. One of the components belongs to a lower resolution space V_{m-1} , while the other to the orthogonal space W_{m-1} that corresponds to the difference signal between the two successive resolutions. Mathematically speaking

$$\begin{aligned} f^m(\tau) &= \sum_n \langle f^m, \phi_{m-1,n} \rangle \phi_{m-1,n} + \sum_n \langle f^m, \psi_{m-1,n} \rangle \psi_{m-1,n} \\ &= \sum_n a^{m-1,n} \phi_{m-1,n} + \sum_n d^{m-1,n} \psi_{m-1,n} \\ &= f^{m-1} + \sum_n d^{m-1,n} \psi_{m-1,n} \end{aligned} \tag{33}$$

Coefficients $a^{m-1,n}$, $d^{m-1,n}$ are called the approximation and the detail coefficients respectively. The function f^{m-1} is an approximation of the function f^m at a lower resolution. The same procedure can be carried out on f^{m-1} and so on, each time reducing the resolution by half and generating an additional set of detail coefficients. The final decomposition, based on Daubechies-4 wavelets consists of only two approximation coefficients and remaining detail coefficients. The refinement Eqs. (26) and (29) can be used to connect the basis functions at the two consecutive resolutions $m-1$ and m . For the Daubechies-4 wavelet, this yields:

$$\begin{aligned} \phi(2^{m-1}\tau - n) &= \sum_{k=1}^4 h_k \phi(2^m\tau - 2n - k) \\ \psi(2^{m-1}\tau - n) &= \sum_{k=1}^4 g_k \psi(2^m\tau - 2n - k) \end{aligned} \tag{34}$$

leading to the connection between the bases:

$$\begin{aligned} \phi_{m-1,n} &= \sum_{k=1}^4 \frac{h_k}{\sqrt{2}} \phi_{m,2n+k} \\ \psi_{m-1,n} &= \sum_{k=1}^4 \frac{g_k}{\sqrt{2}} \phi_{m,2n+k} \end{aligned} \tag{35}$$

The approximation coefficients at resolution $m - 1$ can now be written as:

$$\begin{aligned} a^{m-1,n} &= \langle f(\tau), \phi_{m-1,n} \rangle \\ &= \left\langle f(\tau), \sum_{k=1}^4 \frac{h_k}{\sqrt{2}} \phi_{m,2n+k} \right\rangle \\ &= \sum_{k=1}^4 \frac{h_k}{\sqrt{2}} \langle f(\tau), \phi_{m,2n+k} \rangle \\ &= \sum_{k=1}^4 \frac{h_k}{\sqrt{2}} a^{m,2n+k} \end{aligned} \tag{36}$$

Similarly for the detail coefficients at resolution $m - 1$:

$$d^{m-1,n} = \sum_{k=1}^4 \frac{g_k}{\sqrt{2}} a^{m,2n+k} \tag{37}$$

The above two relationships can be written in matrix form, assuming periodic extensions for the coefficients at resolution m as:

$$\begin{Bmatrix} \mathbf{a}^{m-1} \\ \mathbf{d}^{m-1} \end{Bmatrix} = \frac{1}{\sqrt{2}} \begin{bmatrix} \mathbf{H} \\ \mathbf{G} \end{bmatrix} \mathbf{a}^m \tag{38}$$

where:

$$\begin{bmatrix} \mathbf{H} \\ \mathbf{G} \end{bmatrix} = \begin{bmatrix} h_1 & h_2 & h_3 & h_4 & 0 & 0 & \dots & 0 & 0 \\ 0 & 0 & h_1 & h_2 & h_3 & h_4 & \dots & 0 & 0 \\ \vdots & \vdots \\ h_3 & h_4 & 0 & 0 & 0 & 0 & \dots & h_1 & h_2 \\ g_1 & g_2 & g_3 & g_4 & 0 & 0 & \dots & 0 & 0 \\ 0 & 0 & g_1 & g_2 & g_3 & g_4 & \dots & 0 & 0 \\ \vdots & \vdots \\ g_3 & g_4 & 0 & 0 & 0 & 0 & \dots & g_1 & g_2 \end{bmatrix} \tag{39}$$

The operation in Eq. (38) is similar to the action of a low pass \mathbf{H} filter and a high pass \mathbf{G} filter on the original data, yielding the approximation and detail coefficients respectively. The $m - 1$ level approximation coefficients can be further decomposed into approximation and detail coefficients at resolution $m - 2$, and can be successively continued till $m = 1$. The end results are approximation coefficients at $m = 1$ and detail coefficients at each filtering step. The coefficients are stored in a single array $\{\mathbf{c}\}$ and Table 4 shows the connection to the projection spaces for $m = 7$.

For all linear operations, the multi-resolution decomposition may be represented as:

$$c^k = \sum_{l=1}^{N_{wav}} T_{kl} f(\tau_l) \quad k = 1 \dots N_{wav} \tag{40}$$

where c^k are the wavelet approximation and detail coefficients. The function is sampled at $N_{wav} (= 2^m)$ points in the fine time scale τ_l .

Table 4
Coefficient numbers and resolution space.

Coeff.	c^1-c^2	c^3-c^4	c^5-c^8	c^9-c^{16}	$c^{17}-c^{32}$	$c^{33}-c^{64}$	$c^{65}-c^{128}$
Space	V_1	W_1	W_2	W_3	W_4	W_5	W_6

$\mathbf{T} (= T_{ij} \mathbf{e}_i \otimes \mathbf{e}_j)$ is an orthogonal matrix containing the filter coefficients constructed by repeated application of Eq. (56).

4.1.1. Advantageous wavelet properties

Wavelet functions form excellent bases in the representation of fine time or τ -scale cyclic response patterns, on account of the following properties:

- **Compact support:** Each wavelet basis has a compact support, i.e. spans a finite domain. As a result, the wavelet decomposition does not exhibit spurious instabilities like the Gibbs phenomena, commonly encountered with Fourier series representations.
- **Multi-resolution:** For a given resolution of the fine scale response, the space of basis functions is well defined and finite, unlike in the Fourier basis. This implies that it is a-priori possible to identify known set of wavelet basis functions to represent the fine scale variables in crystal plasticity analysis under cyclic loading. For the Fourier series, this has to be found by trial and error.
- **Number of coefficients:** The number of wavelet terms and coefficients can be minimized for a known response function. For example, in the case of dwell or triangular loading, response functions over a cycle might have segments that are almost linear. This makes the Daubechies-4 wavelets an ideal choice, since they are able to represent linear behavior exactly with only a few coefficients.

Choice of the optimal resolution in the wavelet representation is critical both for accuracy and efficiency of the problem solved. The maximum representative resolution can be obtained from the minimum time step required to integrate the single time scale problem to within a prescribed accuracy. In practice, this is determined from the first few cycles and the same resolution is retained throughout. This assumption is valid as long as there is no sudden change in the loading or boundary conditions in the problem course. For the simulations in the present work, it was observed that a time step of $\frac{1}{27}$ gives a converged solution for the first few cycles and therefore has been used.

4.2. Coarse scale evolutionary constitutive relations

Coarse scale constitutive equations of the form in Eq. (24) are developed in this section. The evolution equation of a state variable y is assumed to be of the form:

$$\dot{y} = f(y, \varepsilon(t)) = f(y, \varepsilon^k(N), \tau) \tag{41}$$

where $\varepsilon^k(N)$ are known wavelet coefficients for the applied strain $\varepsilon(t)$. Given the initial value $y_o(N) = y(N, 0)$ for a cycle N and the wavelet decomposed strain components $\varepsilon^k(N)$, the value of y at any fine time scale point (τ) within the cycle can be expressed as:

$$y(N, \tau) = y(N, 0) + \int_0^\tau f(y, \varepsilon^k(N), \tau') d\tau' = y_o(N) + \int_0^\tau f(y, \varepsilon^k(N), \tau') d\tau' \tag{42}$$

Continuity of y across cycles with time period T yields the relation $y(N, T) = y(N + 1, 0) = y_o(N + 1)$. Consequently, the coarse time scale derivative of y can be expressed as:

$$\frac{dy_o}{dN} = y(N, T) - y(N, 0) = \int_0^T f(y, \varepsilon^k(N), \tau') d\tau' = Y_o(y_o, \varepsilon^k) \tag{43}$$

Eq. (43) represents the rate of change of the initial value of y per cycle, for which the integral expression is evaluated numerically using the backward Euler method. A second order implicit backward difference integration scheme is utilized for integration of this

equation. A multi-time step formalism is adopted in this scheme, where the derivative is expressed as:

$$\frac{dy_o}{dN}(N + \Delta N) = \frac{a_1 y_o(N + \Delta N) - a_2 y_o(N) + a_3 y_o(N - \Delta N_p)}{\Delta N} \quad (44)$$

ΔN and ΔN_p are cycle jumps corresponding to the current and previous steps. The parameters are expressed in terms of the cycle step ratio $r = \frac{\Delta N_p}{\Delta N}$, as:

$$a_1 = \frac{\{(r+1)^2 - 1\}}{\{(r+1)^2 - (r+1)\}}, a_2 = \frac{(r+1)^2}{\{(r+1)^2 - (r+1)\}}, a_3 = \frac{1}{\{(r+1)^2 - (r+1)\}}$$

4.3. Coarse (Cycle) scale crystal plasticity finite element equations

The wavelet transform based multi-time scale (WATMUS) algorithm is applied to the crystal plasticity constitutive models presented in Section 2. The evolving microstructural variables in the crystal plasticity constitutive relations (1)–(7) are: F^p , g^α , χ^α . Applying the methodology discussed in the previous section, the coarse scale evolution equations for these variables can be expressed as:

$$\begin{aligned} \frac{dF_{ij}^{po}}{dN} &= f_{ij}(F_{ij}^k(N), F_{ij}^{po}, g^{\alpha o}, \chi^{\alpha o}) \\ \frac{dg^{\alpha o}}{dN} &= G^\alpha(F_{ij}^k(N), F_{ij}^{po}, g^{\alpha o}, \chi^{\alpha o}) \\ \frac{d\chi^{\alpha o}}{dN} &= B^{\alpha o}(F_{ij}^k(N), F_{ij}^{po}, g^{\alpha o}, \chi^{\alpha o}) \end{aligned} \quad (45)$$

Here F_{ij}^{po} is the initial value of plastic deformation gradient, $g^{\alpha o}$ and $\chi^{\alpha o}$ are the initial values of hardness and back stress respectively for slip system α for the cycle N . The right hand side in Eq. (45) is calculated using the formula in Eq. (43), i.e.:

$$\frac{dF_{ij}^{po}}{dN} = \int_0^T \dot{F}_{ij}^p(N, \tau) d\tau = \int_0^T \sum_{\alpha} \dot{\gamma}^\alpha s_{oi}^\alpha m_{ok}^\alpha F_{kj}^p d\tau \quad (46)$$

The integral in the numerator of the RHS is evaluated numerically using the backward Euler method. Once the values of coarse scale variables are known, the increments of the Cauchy stress $\Delta\sigma(N, \tau)$ and other state variables can be computed over the cycle N .

The finite element formulation for the coarse scale equations introduces wavelet coefficients of nodal displacements as the primary solution variable, as opposed to nodal displacement components in conventional FEM. In this formulation, the element displacement field and the associated generalized nodal displacements of each element are expressed in terms of the wavelet basis expansion as:

$$u_i(\mathbf{X}, N, \tau) = \sum_{\alpha} N_{\alpha}(\mathbf{X}) q_{\alpha i}(N, \tau) = \sum_{\alpha} N_{\alpha}(\mathbf{X}) \sum_k^{N_{wav}} q_{\alpha i}^k(N) \psi_k(\tau) \quad (47)$$

where $N_{\alpha}(\mathbf{X})$ is the shape functions corresponding to the node α , $q_{\alpha i}$ is the nodal displacement component i for the α -th node in an element, and $q_{\alpha i}^k(N); k = 1 \dots N_{wav}$ are the corresponding wavelet coefficients. The wavelet coefficients are functions of N and not of τ , i.e. they evolve in the cycle scale alone. The corresponding wavelet coefficients of the deformation gradient field are derived to be:

$$F_{ij}^k(\mathbf{X}, N) = \int_0^T \left(\delta_{ij} + \frac{\partial u_i}{\partial X_j} \right) \psi_k(\tau) d\tau = \delta_{ij} \int_0^T \psi_k(\tau) d\tau + \sum_{\alpha} \frac{\partial N_{\alpha}(\mathbf{X})}{\partial X_j} q_{\alpha i}^k(N) \quad (48)$$

4.3.1. Starting procedure for solving the cycle scale problem

Initial conditions of the cycle scale governing equations are generated by conducting single (fine) scale analysis for the first few cycles ($N_o \leq 5$). This yields the initial displacement response and the initial values of the wavelet coefficients discussed in Eq. (29), i.e.

$$q_{\alpha i}^k(N_o) = \sum_{l=1}^{N_{wav}} T_{kl} q_{\alpha i}(N_o, \tau_l) \quad k = 1 \dots N_{wav} \quad (49)$$

$q_{\alpha i}^k(N_o)$ s are wavelet coefficients of the nodal displacements resolved over the cycle N_o and N_{wav} corresponds to the number of wavelet basis functions or coefficients. The number of degrees of freedom for the corresponding finite element problem is then $N_d \times N_{wav}$, where N_d is the number of displacement degrees freedom in a conventional single time-scale FEM problem.

5. Adaptivity for accuracy and efficiency in the WATMUS methodology

The accuracy and efficiency of the wavelet transformation based multi-time scaling (WATMUS) methodology depends on two specific parameters, viz. (i) the number (N_{wav}) of wavelet bases or displacement coefficients $q_{\alpha i}^k(N)$ selected in Eq. (47) and (ii) the step size ΔN or the number of cycles traversed in each increment of the numerical integration scheme. Optimally, N_{wav} should be low and ΔN as high as possible, while keeping the net errors due to waveform representation and series truncation respectively to under pre-determined bounds. These criteria are discussed next.

5.1. Evolving and active wavelet basis functions

Retaining all the wavelet basis functions at a given resolution for representing a response function in Eq. (47) may lead to a large number of degrees of freedom in the crystal plasticity FE model. The efficiency of the WATMUS method can benefit significantly from optimally reducing N_{wav} , by incorporating only the active and evolving wavelet bases required to represent the fine scale cyclic behavior of any state variable. The following scheme is developed for adaptively selecting those coefficients that change considerably in time. For a given degrees of freedom, it divides the total set of wavelet coefficients $\mathcal{S}_{\alpha i} = \{q_{\alpha i}^k | k = 1 \dots N_{wav}\}$ into a set of evolving ($\mathcal{S}_{\alpha i}^{evol}$) and non evolving ($\mathcal{S}_{\alpha i}^{no-evol}$) coefficients respectively, i.e. $\mathcal{S}_{\alpha i} = \mathcal{S}_{\alpha i}^{evol} \cup \mathcal{S}_{\alpha i}^{no-evol}$. The division is based on the following criterion.

$$\begin{aligned} \mathcal{S}_{\alpha i}^{evol} &= \{q_{\alpha i}^k | q_{\alpha i}^{k+1} - 2q_{\alpha i}^k + q_{\alpha i}^{k-1} > \eta_1 C_k^{tol}, k = 1 \dots N_{wav}\} \\ &= \{\hat{q}_{\alpha i}^k | k = 1 \dots N_{\alpha i}^{evol}\} \setminus \mathcal{S}_{\alpha i}^{non-evol} = \mathcal{S}_{\alpha i} \setminus \mathcal{S}_{\alpha i}^{evol} \end{aligned} \quad (50)$$

The coefficient $C_k^{tol} = \max_{2^{[log_2 k]} < l < 2^{[log_2 k] + 1}} (c_{l+1} - 2c_l + c_{l-1})$ is the maximum value of all coefficients at each resolution and η_1 is a prescribed tolerance. The variation of nodal displacements over a given cycle can be obtained from its wavelet coefficients using the orthogonality property of the transformation matrix (see Eq. (56)):

$$\begin{aligned} q_{\alpha i}(N, \tau_j) &= \sum_{k=1}^{N_{wav}} T_{kj}^{\alpha i} q_{\alpha i}^k(N) \quad j = 1 \dots N_{wav} \\ &= \sum_{q_{\alpha i}^k \in \mathcal{S}_{\alpha i}^{evol}} T_{kj}^{\alpha i} q_{\alpha i}^k(N) + \sum_{q_{\alpha i}^k \in \mathcal{S}_{\alpha i}^{non-evol}} T_{kj}^{\alpha i} q_{\alpha i}^k(N) \\ &= \sum_{k=1}^{N_{\alpha i}^{evol}} \hat{T}_{kj}^{\alpha i} \hat{q}_{\alpha i}^k(N) + q_{\alpha i}^{add}(\tau_j) \end{aligned} \quad (51)$$

The matrix $\hat{\mathbf{T}}^{\alpha i}$ is constructed from the wavelet transform matrix \mathbf{T} by removing the rows corresponding to the non-evolving coefficients. The non-evolving coefficients remain constant during an integration step and is denoted by $q_{\alpha i}^{add}(\tau_j) = \sum_{q_{\alpha i}^k \in \mathcal{S}_{\alpha i}^{non-evol}} T_{kj}^{\alpha i} q_{\alpha i}^k(N)$.

The primary solution variables, corresponding to the displacement degrees of freedom, for the coarse-scale finite element model are q_{α}^k . Accordingly, the wavelet coefficient degrees of freedom is $\sum_{\alpha=1}^{N_{nodes}} \sum_{i=1}^3 N_{\alpha i}^{evol}$, corresponding to the sum of the number of evolving coefficients for all the displacement components at all nodes α . The unknown wavelet coefficients for a cycle are solved using the standard weak form of the equilibrium equation, decomposed into its wavelet components and expressed as:

$$f_i^k(N) = \sum_{l=1}^{N_{evol}^i} \hat{T}_{kl}^i f_l(N, \tau_l) = 0, \tag{52}$$

where $f_i(N, \tau_l) = \int_{V(\tau_l)} B_{ji} \sigma_j(N, \tau_l) dV - \int_{S_t(\tau_l)} N_{ji} \bar{t}(N, \tau_l) dS$

Here B_{ji} and N_{ji} are matrices that respectively relate the element strain and displacement components to the nodal displacements for the i -th degree of freedom in a conventional, single time scale FEM analysis. Furthermore, $\bar{t}(N, t)$ is the applied load over cycle N . The change in Cauchy stress σ_j in the Voigt form over the N -th cycle is obtained as a function of the nodal displacement components by solving the coarse cycle scale equations. Eqs. (52) are solved using the Newton family of nonlinear iterative solvers, for which the Jacobian matrix is approximated as:

$$\frac{\partial f_i^k}{\partial q_j^l} = \sum_{m=1}^{N_{wav}} \hat{T}_{km}^i \frac{\partial f_i}{\partial q_j}(\tau_m) \hat{T}_{lm}^j \tag{53}$$

It is obtained by transforming the fine time scale Jacobian $\frac{\partial f_i}{\partial q_j}$, for geometrically non-linear problems (see [52]) at a point τ_m , by the wavelet transformation matrix \mathbf{T} . Quasi-Newton non-linear solvers e.g. in [32] are used for solving the nonlinear equations and the expression (53) is used as the initial estimate for the Jacobian matrix.

5.1.1. Procedure for adding and removing wavelet coefficients

Adding and removing wavelet bases for accurate representation of the response functions is important for optimal convergence of the WATMUS method. The procedure for adaptively adding and removing wavelet coefficients $q^k; k = 1 \dots N_{wav}$ is illustrated with a 1-D problem (Section 6.1).

1. Start with an initial guess on the set of evolving coefficients \mathcal{G}^{evol} based on a selection criterion. In the case of the 1-D problem the criterion used is: $\mathcal{G}^{evol} = \{k | \frac{dq^k}{dN} \geq c_{tol} \times \max_l |q^l|\}$ and $\mathcal{G}^{non-evol} = \mathcal{G} \setminus \mathcal{G}^{evol}$.
2. Solve the problem for the evolving coefficients:

$$f^k(q^l) = 0 \quad \forall (k, l) \in \mathcal{G}^{evol} \times \mathcal{G}^{evol} \tag{54}$$

3. Based on the solution, select the set of coefficients \mathcal{G}^{add} to be added according to the criterion:

$$\mathcal{G}^{add} = \{q^k | q^k \in \mathcal{G}^{non-evol} \text{ and } |f_k| > \eta_F\} \tag{55}$$

It implies all non-evolving coefficients, whose residual is greater than a tolerance η_F given by the maximum value of the converged residual corresponding to the evolving coefficients, are selected. If $\mathcal{G}^{add} \neq \emptyset$, then $\mathcal{G}^{evol} = \mathcal{G}^{evol} \cup \mathcal{G}^{add}$.

- 4 Go to Step 1.

This procedure ensures that an appropriate set of displacement coefficients are selected such that all the wavelet coefficients of the residual are within a certain tolerance, as opposed to just the ones corresponding to the evolving set. This in turn guarantees that the error in the displacement coefficients remain bounded as a consequence of the lemma discussed below.

Lemma 1. Let q_{exact}^k denote the exact solution for the wavelet coefficients and q^k be the solution obtained by the dual time WATMUS framework procedure for the cycle N by solving only in \mathcal{G}^{evol} . Then

$$|q_{exact}^k - q^k| \leq N_{wav} \max_{p \in \mathcal{G}} |K_{kp}^{-1}(\xi)| \max_{l \in \mathcal{G}} |f_l| \quad \forall k \in \mathcal{G} \tag{56}$$

where $K_{ij} = \frac{\partial f_i}{\partial q_j}$ and $\xi_k \in (q^k, q_{exact}^k)$.

Proof. Using the Taylor expansion of f^k about q^k :

$$f^k(q_{exact}) = f^k(q) + \sum_{l=1}^{N_{wav}} \frac{\partial f^k}{\partial q^l}(\xi) (q_{exact}^l - q^l) \tag{57}$$

with $\xi_l \in (q^l, q_{exact}^l)$. Note that the dual time scale procedure solves $f^k = 0$ for $q^k \in \mathcal{G}^{evol}$. The exact solution however needs to satisfy:

$$f_k(q_{exact}^l) = 0 \quad \forall k, l \in \mathcal{G} \tag{58}$$

Assuming the solution is unique, Eq. (57) can be used to obtain:

$$q_{exact}^k - q^k = \sum_{l=1}^{N_{wav}} K_{kl}^{-1}(\xi) f_l, \text{ where } K_{kl} = \frac{\partial f^k}{\partial q^l} \tag{59}$$

The Cauchy Schwarz inequality yields:

$$|q_{exact}^k - q^k| \leq \sqrt{\sum_{p=1}^{N_{wav}} (K_{kp}^{-1})^2} \|f\| \tag{60}$$

This completes the proof as:

$$|q^k - q_{exact}^k| \leq N_{wav} \max_{p \in \mathcal{G}} |K_{kp}^{-1}(\xi)| \max_{l \in \mathcal{G}} |f_l| \quad \forall k \in \mathcal{G} \tag{61}$$

Numerically, it has been observed that $|K_{kp}^{-1}| < 1$. Thus, the above lemma ensures that the error in all wavelet coefficients remain bounded even when solving with a reduced set \mathcal{G}^{evol} , as long as the error in all the residuals belonging to \mathcal{G} remain bounded.

The procedure developed can be combined with a criterion for removing coefficients to obtain the optimal set of evolving coefficients. Coefficients whose cyclic rate of change is less than a pre-set tolerance (η_{del}) are removed from \mathcal{G}^{evol} i.e.

$$\begin{aligned} \mathcal{G}^{non-evol} &= \mathcal{G}^{non-evol} \cup \{q^k | |q^k(N)q^k(N-\Delta N)| / \Delta N \leq \eta_{del} \max_{\mathcal{G}^{evol}} |q^l|\} \\ \mathcal{G}^{evol} &= \mathcal{G} \setminus \mathcal{G}^{non-evol} \end{aligned} \tag{62}$$

This yields the new set of evolving coefficients.

5.2. Coarse (Cycle scale) integration step size control

The step size in the integration of cycle scale equations corresponds to the number of cycles traversed in each increment of the numerical integration scheme. An optimal step size is estimated in the WATMUS method from a truncation error criterion in conjunction with the residual of the equilibrium equation. For the implicit second order backward difference scheme in Eq. (44), the truncation error criterion is derived from the truncation of second order terms in the Taylor's expansion of variable y_0 as:

$$\delta y_0 = \frac{1}{6} \left| \frac{d^3 y}{dN^3} \frac{(r+1)^2 - (r+1)^3}{(r+1)^2 - 1} \right| \Delta N^3 \tag{63}$$

where $r = \frac{\Delta N_p}{\Delta N}$ is the ratio of the previous to the current step size. The relative error, plotted as a function of r in Fig. 8, shows that the error decreases asymptotically as r increases.

The norm of the error that is propagated to the equilibrium residual δf from the constitutive level truncation error (63), is derived as:

$$\delta f = \delta f_{err} \Delta N^3, \quad \text{where } \delta f_{err} = \frac{1}{6} \max_{el} \left\| \int_{V_{el}} \mathbf{B}^T \frac{\partial \sigma}{\partial \mathbf{F}^{po}} \frac{(r+1)^2 - (r+1)^3 d^3 \mathbf{F}^{po}}{(r+1)^2 - 1} \frac{d^3 \mathbf{F}^{po}}{dN^3} dV \right\| \quad (64)$$

Eq. (64) accounts for the effect of the local constitutive error on the global equilibrium equations in the coarse scale problem. For the error to be bounded by a prescribed relative tolerance η , the maximum allowed cycle step jump ΔN_{jump} is estimated as:

$$\Delta N_{jump} \leq \left(\frac{6\eta f_{err}}{\delta f_{err}} \right)^{\frac{1}{3}}, \quad \text{where } f_{err} = \sum_{el} \left\| \int_{V_{el}} \mathbf{B}^T \frac{\partial \sigma}{\partial \mathbf{F}^{po}} dV \right\| \quad (65)$$

6. Numerical examples solved with the WATMUS algorithm

The wavelet transformation based multi-time scaling (WATMUS) methodology is applied to study the cyclic response of a one dimensional viscoplastic problem and a three-dimensional rate dependent crystal plasticity problem discussed next.

6.1. 1-dimensional elastic-viscoplastic problem

The WATMUS methodology is applied to study cyclic response of a 1-D elastic-viscoplastic bar introduced in Section 3. The bar is fixed at the left end and is subjected to a sinusoidal loading at the right end with frequency $\omega = 2\pi$, i.e. period $T = 1$ s. Variables in Eq. (10) that are integrated using the second order backward difference algorithm in Eq. (44) are the initial values of the plastic strain (ϵ^{po}) and hardness (g^o). For the 1-D problem, the algorithm is written as:

$$\mathbf{f}^{const} = a_1 \alpha_o(N + \Delta N) - a_2 \alpha_o(N) + a_3 \alpha_o(N - \Delta N_p) - \Delta N \frac{d\alpha_o}{dN}(N + \Delta N) = 0 \quad (66)$$

where $\alpha_o = \begin{Bmatrix} \epsilon^{po} \\ g^o \end{Bmatrix}$

Derivatives in Eq. (66) are calculated using Eq. (43). The Newton-Raphson nonlinear solver is used to calculate $\alpha_o(N + \Delta N)$ from

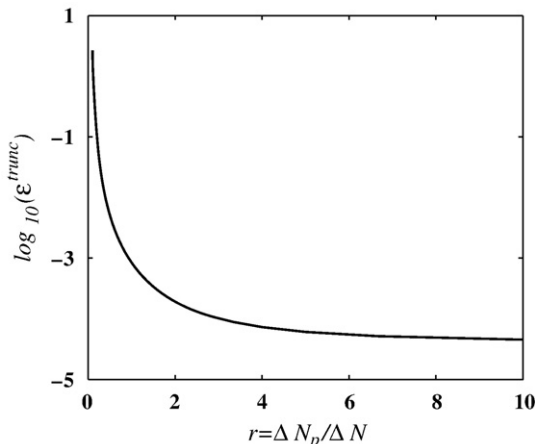


Fig. 8. Variation of truncation error $\epsilon^{trunc} = \frac{\epsilon^{po}_{integrated} - \epsilon^{po}_{exact}}{\epsilon^{po}_{exact}}$ with step size ratio r .

Eq. (66). The only unknown displacement in the model is that of node 2 (between the two elements), which is decomposed into its wavelet coefficients. The equilibrium equation, resolved in the wavelet basis, over a cycle step at $N + \Delta N$ is:

$$f^k(N + \Delta N) = \sum_{l=1}^{N_{wav}} \hat{T}_{kl} [\sigma_1(N + \Delta N, \tau_l) - \sigma_2(N + \Delta N, \tau_l)] = 0, \quad k = 1 \dots N_{evol} \quad (67)$$

where σ_i corresponds to the stress in element i and N_{evol} is the number of evolving displacement coefficients. The criterion for the maximum integration step-size is obtained similar to Eq. (65).

6.1.1. Jacobian matrices for solving the viscoplastic equations

Jacobian matrices for the constitutive level and equilibrium level iterations for the 1-D model are derived here. The evolving state variables during the cycle $N + \Delta N$ are:

$$\alpha(N + \Delta N, \tau) = \begin{Bmatrix} \epsilon^p(N + \Delta N, \tau) \\ g(N + \Delta N, \tau) \end{Bmatrix} \quad (68)$$

The corresponding coarse time variables are denoted as:

$$\alpha_o(N + \Delta N) = \alpha(N + \Delta N, 0) = \begin{Bmatrix} \epsilon^p(N + \Delta N, 0) \\ g(N + \Delta N, 0) \end{Bmatrix} = \begin{Bmatrix} \epsilon^{po}(N + \Delta N) \\ g^o(N + \Delta N) \end{Bmatrix} \quad (69)$$

Coarse scale derivatives of these variables are obtained from Eq. (61) as:

$$\frac{d\alpha_o}{dN}(N + \Delta N) = \alpha(N + \Delta N, T) - \alpha(N + \Delta N, 0) = \alpha(N + \Delta N, \tau_{N_{wav}}) - \alpha(N + \Delta N, 0) \quad (70)$$

where N_{wav} is the number of fine-scale points used to sample the displacement field at node 2. With a known value of α_o , the backward Euler method is applied to the integral Eq. (43) to obtain $\alpha_{N_{wav}}$ from Eq. (10) as:

$$\alpha_k = \alpha_{k-1} + \dot{\alpha}_k \Delta \tau \Rightarrow \begin{Bmatrix} \epsilon_k^p \\ g_k \end{Bmatrix} = \begin{Bmatrix} \epsilon_{k-1}^p \\ g_{k-1} \end{Bmatrix} + \begin{Bmatrix} \dot{\alpha} \Delta \tau \left| \frac{\sigma_k}{g_k} \right|^{\frac{1}{m}} \text{sign}(\sigma_k) \\ h \left| \epsilon_k^p - \epsilon_{k-1}^p \right| \end{Bmatrix} \quad (71)$$

The subscript k refers to the variable evaluated at fine-scale point τ_k with $k = 1 \dots N_{wav}$, and $\Delta \tau = \frac{1}{N_{wav}}$. Linearization of the above equation yields:

$$d\alpha_k = \mathbf{A}_k d\alpha_{k-1} + \begin{Bmatrix} EB_\gamma / g_k \\ h \text{sign}(\sigma_k) \end{Bmatrix} d\epsilon \quad \text{where}$$

$$\mathbf{A}_k = \frac{\partial \alpha_k}{\partial \alpha_{k-1}} = \left(\mathbf{I} - \begin{bmatrix} -EB_\gamma / g_k & -B_\gamma \sigma_k / g_k^2 \\ h \text{sign}(\sigma_k) & 0 \end{bmatrix} \right)^{-1} \times \begin{bmatrix} 1 & 0 \\ -h \text{sign} \sigma_k & 1 \end{bmatrix} \quad \text{and} \quad B_\gamma = \frac{\dot{\alpha} \Delta \tau}{m} \left| \frac{\sigma}{g} \right|^{\frac{1}{m}-1} \quad (72)$$

For iteratively solving the constitutive level equations, the applied strain is kept fixed, i.e. $d\epsilon_k = 0$ for all k . Applying chain rule to Eq. (72) yields the relation:

$$\frac{d\alpha_k}{d\alpha_o} \Big|_\epsilon = \prod_{l=0}^k \mathbf{A}_l \quad \text{with} \quad \mathbf{A}_0 = \mathbf{I}, \quad k = 1 \dots N_{wav} \quad (73)$$

Linearizing the constitutive residual Eq. (66) and substituting into Eq. (70) results in:

$$d\mathbf{f}^{const} = b_\gamma d\alpha_o - \Delta N d\alpha_{N_{wav}} \quad \text{where } b_\gamma = (a_1 + \Delta N) \quad (74)$$

Substituting Eq. (73) into the above equation yields the Jacobian for the iterative solution of the constitutive relations as:

$$\frac{d\mathbf{f}^{const}}{d\alpha_o} = b_\gamma \mathbf{I} - \Delta N \prod_{l=0}^{N_{wav}} \mathbf{A}_l \quad (75)$$

For calculating the Jacobian in the iterative solution of the equilibrium equation, it is linearized with respect to the node 2 displacement coefficients. In this case, the applied strain is perturbed as:

$$d\epsilon_k = \sum_{l=1}^{N_{evol}} \hat{T}_{lk} d\hat{q}_l \quad (76)$$

where \hat{T}_{kl} are components of the wavelet transformation matrix in Eq. (49) and \hat{q}_l are the evolving displacement coefficients at node 2. Substituting Eqs. (72) and (73) into Eq. (76) yields:

$$\frac{\partial \alpha_k}{\partial \hat{\mathbf{q}}} = \frac{\partial \alpha_k}{\partial \alpha_o} \Big|_\epsilon \frac{\partial \alpha_o}{\partial \hat{\mathbf{q}}} + \mathbf{A}_k \left\{ \frac{B_\gamma E / g_k}{h \text{sign}(\sigma_k)} \right\} \left[\hat{T}_{1k} \dots \hat{T}_{N_{evol}k} \right] \quad (77)$$

The constitutive relations are assumed to be satisfied during equilibrium iteration. consequently, setting $d\mathbf{f}^{const} = 0$ yields the relation:

$$d\alpha_o = \frac{\Delta N}{b_\gamma} d\alpha_{N_{wav}} \quad (78)$$

This is used along with Eq. (77) for $k = N_{wav}$ to obtain:

$$\frac{\partial \alpha_o}{\partial \hat{\mathbf{q}}} = \left(\mathbf{I} - \frac{\Delta N}{b_\gamma} \frac{\partial \alpha_{N_{wav}}}{\partial \alpha_o} \Big|_\epsilon \right)^{-1} \mathbf{A}_{N_{wav}} \left\{ \frac{B_\gamma E / g_k}{h \text{sign}(\sigma_{N_{wav}})} \right\} \left[\hat{T}_{1N_{wav}} \dots \hat{T}_{N_{evol}N_{wav}} \right] \quad (79)$$

Eqs. (77) and (79) are now used to obtain the rate of change of the state variables α_k at a fine time-scale point τ_k with respect to the nodal wavelet coefficients, i.e.

$$\frac{d\alpha_k}{d\hat{\mathbf{q}}} = \left\{ \begin{array}{l} \frac{d\epsilon_k^p}{d\hat{\mathbf{q}}} \\ \frac{dg_k}{d\hat{\mathbf{q}}} \end{array} \right\} \quad (80)$$

This is then used along with the linearized equilibrium Eq. (67) to obtain its Jacobian as:

$$\frac{\partial f^i}{\partial q^j} = 2E\delta_{ij} + E \sum_{l=1}^{N_{wav}} \hat{T}_{il} \left(\frac{\partial \epsilon_l^p}{\partial q_j} \Big|_{elem2} - \frac{\partial \epsilon_l^p}{\partial q_j} \Big|_{elem1} \right) \quad (81)$$

6.1.2. Results of cyclic loading simulation of the 1-D viscoplastic bar problem

The 1-D viscoplastic bar model, described in Section 3 is subjected to a fully reversed ($R = -1$) sinusoidal loading for 2000 cycles. The WATMUS method is used to integrate the problem in coarse cycle scale and the results are compared with those obtained from a single (fine) time-scale analysis, both with respect to accuracy and efficiency. The effects of (i) evolving wavelet coefficients of nodal displacements that are adaptively chosen for a tolerance $ctol$, and

(ii) the maximum allowed step size (number of cycles), on the solution are also investigated.

Three displacement tolerances, viz. $ctol = 10^{-10}$, 10^{-4} , and 10^{-3} are considered for selecting the number of coefficients that are expected to evolve during the loading process. The tolerances result in 128, 30 and 10 initial coefficients respectively, which can evolve freely with deformation. For each of the three tolerances, four different bounds on the maximum cycle step size ΔN_{max} in Eq. (65) are considered. The step size for a coarse scale integration increment is assessed as $\Delta N = \min(\Delta N_{jump}, \Delta N_{max})$. The value of η in Eq. (65) is set to be 10^{-3} . Fig. 9 shows the variation of the coarse scale variables (ϵ^{p0} and g^0) as functions of the number of cycles N .

Once the coarse scale variables (ϵ^{p0} and g^0), along with the wavelet displacement coefficients are known for a given cycle N , the fine scale response for that cycle can be calculated by superimposing the wavelet bases according to in Eq. (42). This is shown in Fig. 10, in which the plastic strain response over the 2000th cycle is obtained from the coarse scale solution. The fine scale response is plotted for different step bounds ΔN_{max} and for different number of evolving coefficients $\hat{\mathbf{q}}$. Excellent agreement is observed between the coarse scale and the single (fine) time-scale results, except for the case with

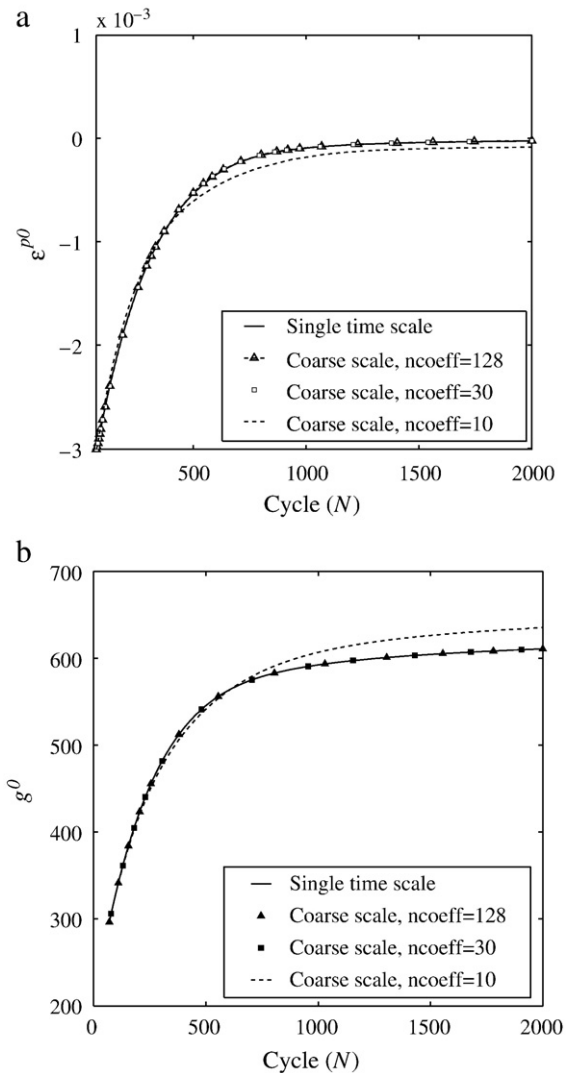


Fig. 9. Evolution of coarse scale variables as a function of cycles (N): (a) initial plastic strain for element 1 with $\Delta N_{max} = 277$, (b) initial hardness for element 1 with $\Delta N_{max} = 25$.

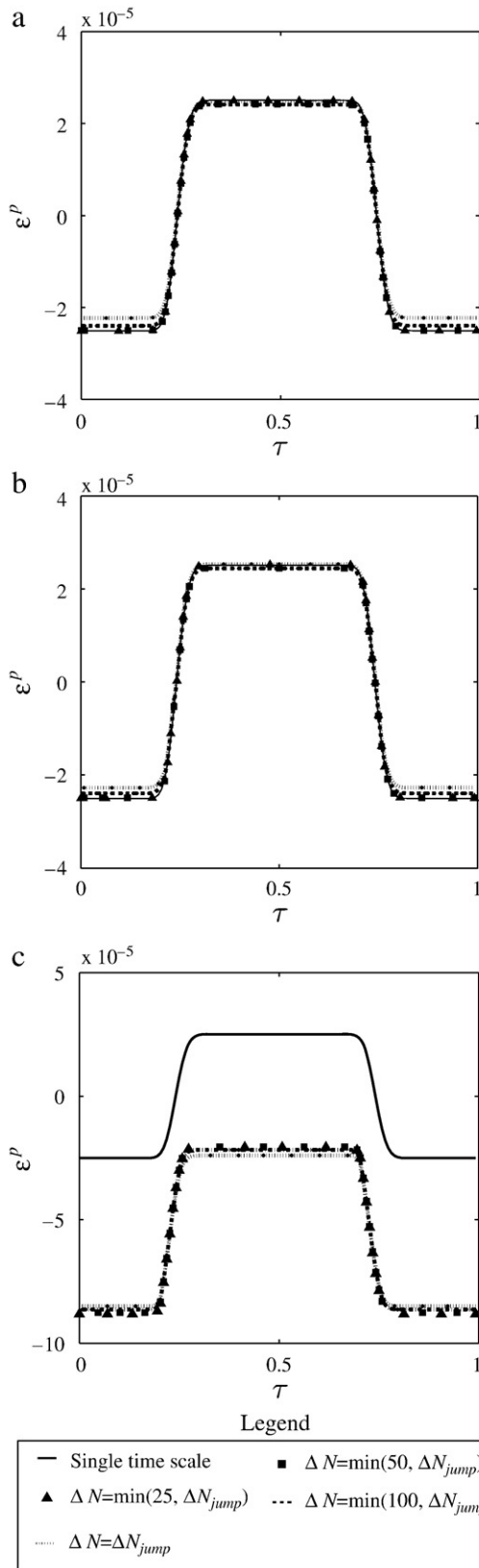


Fig. 10. Reconstructed profile of the fine-scale plastic strain response at the 2000-th cycle for different values of ΔN_{\max} , constructed with: (a) 128 wavelet coefficients, (b) 30 wavelet coefficients, and (c) 10 wavelet coefficients. ΔN_{jump} obtained from Eq. (65).

very few (~ 10) evolving wavelet coefficients which suffers from a significant error regardless of the refinement in the time step as seen from Fig. 10(c). This is due to the fact that there are not enough basis

Table 5

Effect of step size ΔN and number of coefficients \hat{q} on error and efficiency at $N_f=2000$.

Coefficient tolerance	ncoeff	ΔN_{\max}	$\frac{\ e_{\text{course}}^p(N_{\text{wav}}, \tau) - e_{\text{fine}}^p(N_{\text{wav}}, \tau)\ }{\ e_{\text{fine}}^p(N_{\text{wav}}, \tau)\ } (\%)$	Speedup
10^{-10}	128	25	0.336	29
10^{-10}	128	50	2.544	43
10^{-10}	128	100	4.11	58
10^{-10}	128	255	8.11	67
10^{-4}	30	25	1.05	35
10^{-4}	30	50	1.89	53
10^{-4}	30	100	3.73	72
10^{-4}	30	277	6.87	84
10^{-3}	10	25	232.4	36
10^{-3}	10	50	230.8	57
10^{-3}	10	100	229.8	74
10^{-3}	10	214	230.8	83

functions available to represent the displacement response accurately, regardless of the time step. However the accuracy increases rapidly, and the difference in response between reconstructions with 30 and 128 evolving coefficients is minimal. This justifies the development of the criterion in Section 5.1.1 that can yield an optimal number of evolving coefficients during the loading process while retaining accuracy. Table 5 shows the effects of the number of coefficients on the computational speed up and accuracy, compared with the single (fine) time-scale analysis. A computational speedup of approximately 80 times is obtained with comparable accuracy for this problem. Results in the table demonstrate that the number of coefficients used in the solution plays a crucial role in the accuracy of the solution. To ensure that all the required coefficients are included during the loading process, the criterion developed in Section 5.1 especially in Eqs. (54) and (55), is utilized for the problem. The starting list of coefficients are obtained using $ctol = 10^{-3}$. Note that while coefficients chosen based on $ctol$ alone can give large errors, substantial improvement in accuracy can be achieved through the implementation of the adding-removal algorithm in Section 5.1.1. The results of this adaptive procedure are illustrated in Fig. 11(a) and (b). Excellent agreement is observed with the fine scale results. The corresponding number of selected evolving coefficients is shown in Fig. 11(c).

6.2. 3D crystal plasticity FE simulation under cyclic loading

The WATMUS methodology is used in this example to simulate cyclic deformation of the Ti-6Al alloy using the 3D crystal plasticity finite element (CPFE) model discussed in Section 2. A model problem of a polycrystalline microstructure is developed, consisting of 27 cubic grains with different crystallographic orientations. Each grain is subdivided into 27 brick elements resulting in a total of 729 elements for the CPFE model. Euler angles, corresponding to the crystallographic orientation distribution for the model are depicted in Fig. 12. Material parameters for the crystal plasticity model are provided in Section 2. The model is subjected to cyclic loading with a mean stress of 500 MPa, together with a superposed oscillatory portion with a peak of 350 MPa and time period of $T = 1$ s. To start the problem with appropriate values of cycle-derivatives, a fine-scale simulation of the CPFE model is carried out for the first 6 cycles. Thereafter, the coarse-scale WATMUS method is commenced. The starting value of cycle jump is taken as $\Delta N_{\text{jump}} = 2$, while the subsequent cycle steps with loading is obtained from the criterion in Eq. (65) with $\eta = 10^{-2}$. The Daubechies-4 wavelet basis is used to decompose the nodal displacement components in each cycle according to Eq. (47). The value of η_1 in Eq. (50) is set to 10^{-3} in the present simulations. This criterion selects coefficients from regions having rapid fluctuations in values of the response functions and those that are most likely to change as the problem progresses leading to a total of 116,521

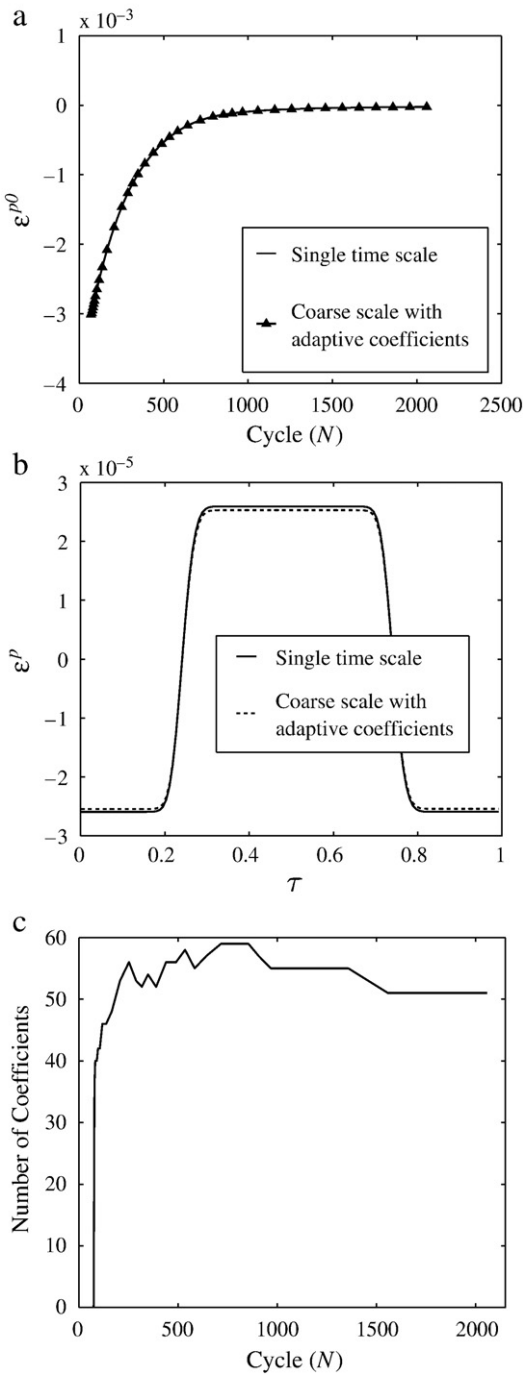


Fig. 11. Effect of adaptive wavelet coefficient inclusion: (a) coarse scale plastic strain as a function of cycle number N , (b) reconstructed plastic strain response with $\Delta N = \min(100, \Delta N_{jump})$ at the 2000-th cycle, and (c) number of evolving coefficients with increasing cycles N .

coefficients with an average of 39 coefficients per degree of freedom for the present problem. Due to the computational cost, the Jacobian matrix is factored at the start of the simulation and is used as the initial Jacobian estimate for every iteration cycle of the quasi-Newton method solution of the equilibrium equations. This is observed to be a good estimate due to the monotonic response of the evolving displacement coefficients.

The simulation is run for only 1000 cycles, so that results can be compared with results from computationally exhaustive single (fine scale) simulations. Fig. 13 shows a comparison of the cycle-scale plastic deformation gradient F^{p0} by coarse and fine time-scale

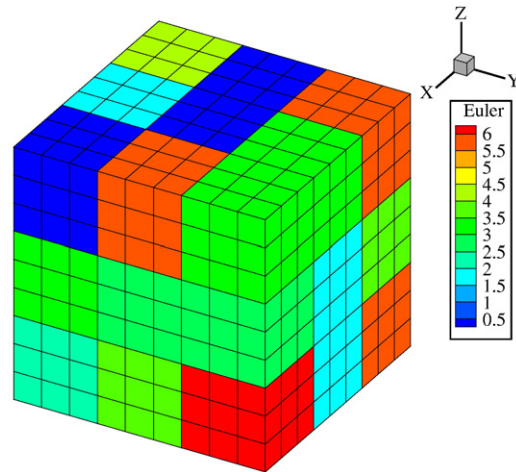


Fig. 12. Euler angle distribution for the 729 element crystal plasticity FE model.

simulations at a typical material point in a grain as a function of the number of cycles. The results of the two methods are indistinguishable for the range considered. The state of stress σ_{zz} in the microstructure along the loading direction at the 1000th cycle is shown in Figs. 14 and 15 for both coarse and fine time scale simulations. As is observed, the coarse time scale and fine time-scale results are in excellent agreement with each other.

Once the coarse scale variables for a given cycle are known, the fine scale response over that cycle can be reconstructed as shown in Fig. 16. A computational time advantage of approximately 7 times is observed for the current problem. The predicted cycle jump ΔN_{jump} from Eq. (65) is expected to increase as the problem progresses due to stabilization of the response, resulting in even higher computational savings.

7. Conclusions

This paper develops a novel wavelet transformation based multi-time scaling (WATMUS) method for crystal plasticity finite element simulations of cyclic deformation in polycrystalline materials leading to fatigue failure. The need for the multi-time scaling is motivated by the large number of cycles that may be required to initiate a fatigue crack in a polycrystalline sample. Simulating such large number of cycles remains intractable to conventional single time scale finite

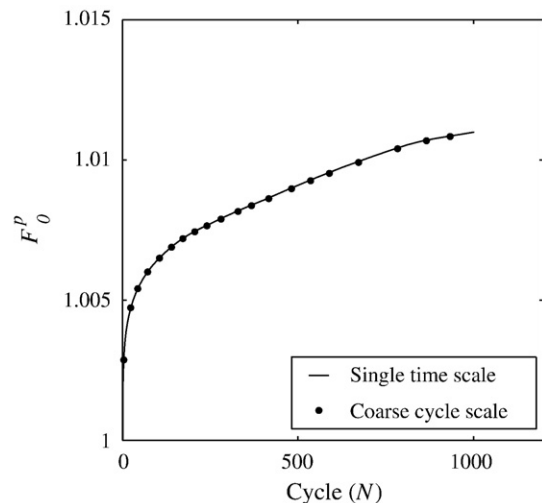


Fig. 13. Coarse scale evolution of plastic deformation gradient F^{p0} as a function of cycle number N .

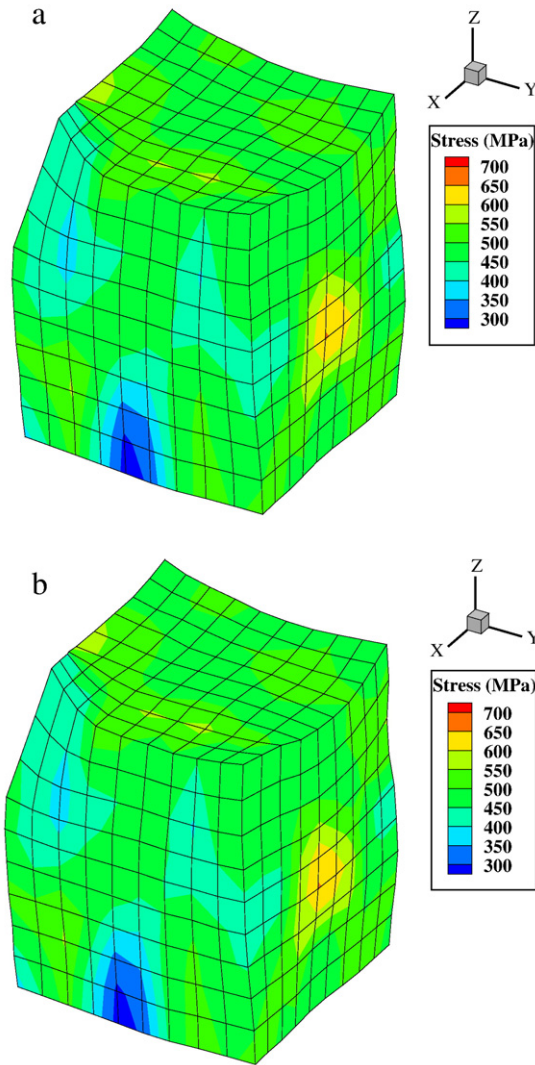


Fig. 14. Stress (σ_{33}) contour for 729 element crystal plasticity by: (a) multi time-scale simulations and (b) fine time-scale simulations.

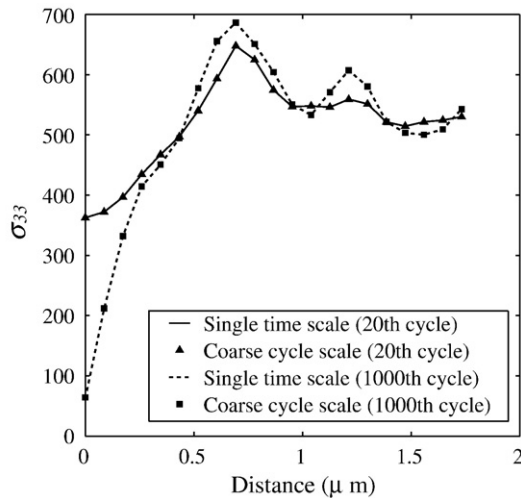


Fig. 15. Variation of stress along the diagonal of the model cube (729 element case).

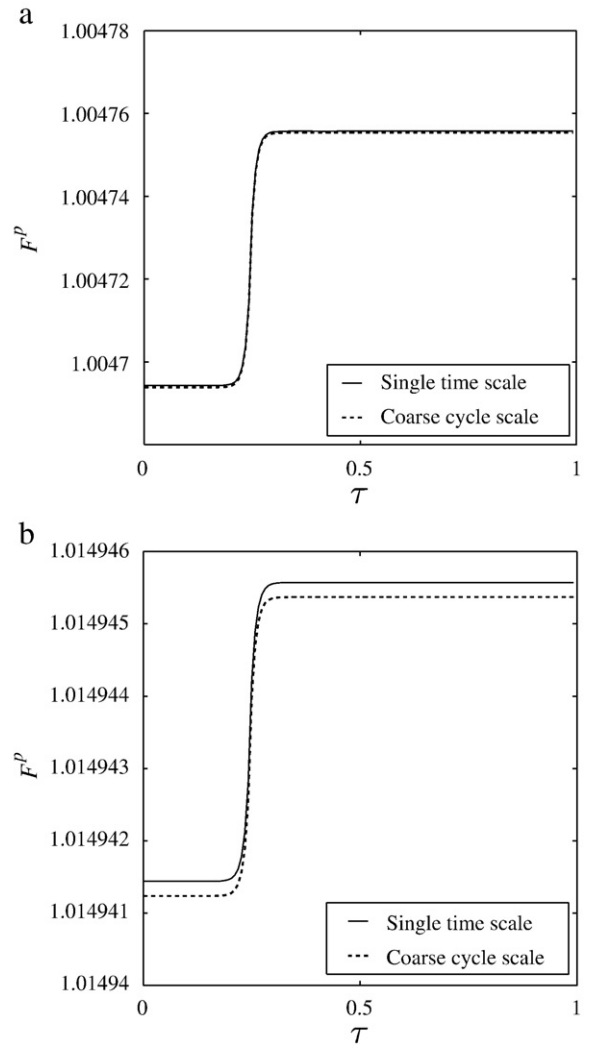


Fig. 16. Reconstructed value of the initial plastic deformation gradient (F_{33}^p) at the (a) 20th cycle and (b) 1000th cycle.

element analysis. The unique aspect of the proposed method is that the algorithm does not require inherent scale separation as with other conventional methods that assume averaging, periodicity or near periodicity. These methods are particularly severely limited in the fully reversed or nearly full reversible range of loading conditions.

The WATMUS methodology introduces wavelet decomposition of nodal displacements and all associated variables in the finite element formulation to decouple the response into a monotonic coarse cycle-scale behavior and a oscillatory fine time scale behavior within each cycle. Multi-resolution wavelet bases functions are effectively able to capture the rapidly varying fine scale response, which necessitates very small time steps in conventional single time scale FEM simulations. An effective criterion is developed for selecting an optimal number of wavelet coefficients in the representation of all response functions in the crystal plasticity simulations. The wavelet transformation is utilized to obtain the coarse scale evolution equations for the microstructural state variables. A novel finite element framework required to incorporate these coarse scale equations is also developed. The coarse scale variables exhibit monotonic behavior, that especially stabilizes with saturating hardness at higher levels of deformation. Relatively large increments, traversing several cycles at a time, can therefore be utilized in the numerical integration scheme with significantly enhanced efficiency. The present numerical simulations exhibit approximately 80–100

times speed-up, even with relatively low number of cycles. Subsequently, fine scale variations in temporal response at any point in a microstructural point can be recovered from values of the nodal displacement wavelet coefficients and the coarse scale state variables at that point. Such fine scale information on microstructural state variables is often required in predicting crack nucleation in the microstructure [13,14,28]. The cyclic response of a 1-D viscoplastic model under fully reversible loading conditions and a representative 3-D crystal plasticity model with cyclic loading conditions are studied using the WATMUS method. The results are in excellent agreement with that of single time scale FEM simulations, while obtaining several fold improvement in the computational time. The overall WATMUS scheme is currently being implemented for predicting fatigue crack nucleation in real metallic materials under field loading conditions.

Acknowledgments

This work has been supported by the US National Science Foundation (Grant # CMMI-0800587, Program Manager: Dr. Clark Cooper), and Office of Naval Research (Grant # N00014-05-1-0504, Program Manager: Dr. Julie Christodolou). This sponsorship is gratefully acknowledged. Computer support by the Ohio Supercomputer Center through grant PAS813-2 is also gratefully acknowledged.

References

- [1] S. Suresh, *Fatigue of Materials*, Cambridge University Press, Cambridge, 1998.
- [2] L.F. Coffin, *Fatigue*, Ann. Rev. Matls. Sci. 2 (1973) 313–348.
- [3] C.M. Laird, The fatigue limit of metals, Mater. Sci. Eng. 22 (1976) 231–236.
- [4] N.A. Fleck, K.J. Kang, M.F. Ashby, The cyclic properties of engineering materials, Acta Metall. Mater. 42 (1994) 365–381.
- [5] T.M. Hashimoto, M.S. Pereira, Fatigue life studies in carbon dual-phase steels, Int. J. Fatigue 18 (8) (1996) 529–533.
- [6] P.C. Paris, *The Fracture Mechanics Approach to Fatigue*, Fatigue—An Interdisciplinary Approach, Syracuse University Press, Syracuse, 1964.
- [7] R.S. Fredell, Operational Needs for a Paradigm Shift in Life Prognosis, Workshop on Prognosis of Aircraft and Space Devices, Components, and Systems, University of Cincinnati, Cincinnati, Ohio, 2008.
- [8] D.C. Lord, L.F. Coffin, Low cycle fatigue hold time behavior of cast Rene 80, Metall. Trans. 4 (1973) 1647–1653.
- [9] H. Tsuji, T. Kondo, Strain–time effects in low cycle fatigue of Nickel-based heat resistant alloys at high temperature, J. Nucl. Mater. 190 (1987) 259–265.
- [10] S.D. Antolovich, S. Liu, R. Baur, Low cycle fatigue behavior of Rene 60 at elevated temperature, Metall. Trans. 12A (1981) 473–481.
- [11] M. Mineur, P. Villechaise, J. Mendez, Influence of the crystalline texture on the fatigue behavior of a 316L austenitic stainless steel, Mater. Sci. Eng. A286 (2000) 257–268.
- [12] V.P. Bennett, D.L. McDowell, Polycrystal orientation distribution effects on microslip in high cycle fatigue, Int. J. Fatigue 25 (2003) 27–39.
- [13] K. Kirane, S. Ghosh, M. Groeber, A. Bhattacharjee, Crystal plasticity finite element based grain level crack nucleation criterion for Ti-6242 alloys under dwell loading, J. Eng. Mater. Technol. ASME 131 (2009) 27–37.
- [14] M. Anahid, P. Chakraborty, D.S. Joseph, S. Ghosh, Wavelet decomposed dual-time scale crystal plasticity FE model for analyzing cyclic deformation induced crack nucleation in polycrystals, Model. Simul. Mater. Sci. Eng. 17 (2009) 064009.
- [15] R.Q. Chu, Z. Cai, S.X. Li, Z.G. Wang, Fatigue crack initiation and propagation in an iron polycrystals, Mater. Sci. Eng. 313 (2001) 61–68.
- [16] S.V. Harren, R.J. Asaro, Nonuniform deformations in polycrystals and aspects of the validity of the Taylor model, J. Mech. Phys. Solids 37 (2) (1989) 191–232.
- [17] K.K. Mathur, P.R. Dawson, U.F. Kocks, On modeling anisotropy in deformation processes involving textured polycrystals with distorted grain shape, Mech. Mater. 10 (1990) 183–202.
- [18] S.R. Kalidindi, C.A. Bronkhorst, L. Anand, On the accuracy of the Taylor assumption in polycrystalline plasticity, in: J.P. Boehler, A.S. Khan (Eds.), *Anisotropy and Localization of Plastic Deformation*, Elsevier Applied Science, London, 1991, pp. 139–142, New York.
- [19] S.R. Kalidindi, C.A. Bronkhorst, L. Anand, Crystallographic texture evolution in bulk deformation processing of fcc metals, J. Mech. Phys. Solids 40 (1992) 537–569.
- [20] A.J. Beaudoin, H. Mecking, U.F. Kocks, Development of local shear bands and orientation gradients in fcc polycrystals, in: S.F. Shen, P.R. Dawson (Eds.), *Simulation of Materials Processing; Theory, Methods and Applications*, NUMIFORM'95, A.A. Balkema, Rotterdam, 1995, pp. 225–230.
- [21] H.S. Turkmen, R.E. Loge, P.R. Dawson, M. Miller, On the mechanical behavior of AA 7075-T6 during cyclic loading, Int. J. Fatigue 25 (2003) 267–281.
- [22] P.R. Dawson, Computational crystal plasticity, Int. J. Solids Struct. 37 (2000) 115–130.
- [23] V. Hasija, S. Ghosh, M.J. Mills, D.S. Joseph, Modeling deformation and creep in Ti-6Al alloys with experimental validation, Acta Mater. 51 (2003) 4533–4549.
- [24] D. Deka, D.S. Joseph, S. Ghosh, M.J. Mills, Crystal plasticity modeling of deformation and creep in polycrystalline Ti-6242, Metall. Trans., A. 17A (5) (2006) 1371–1388.
- [25] G. Venkatramani, D. Deka, S. Ghosh, Crystal plasticity based FE model for understanding microstructural effects on creep and dwell fatigue in Ti-6242, ASME Jour. Engng. Mater. Tech. 128 (3) (2006) 356–365.
- [26] G. Venkatramani, S. Ghosh, M.J. Mills, A size dependent crystal plasticity finite element model for creep and load-shedding in polycrystalline Titanium alloys, Acta Mater. 55 (2007) 3971–3986.
- [27] G. Venkatramani, K. Kirane, S. Ghosh, Microstructural parameters affecting creep induced load shedding in Ti-6242 by a size dependent crystal plasticity FE model, Int. J. Plast. 24 (2008) 428–454.
- [28] K. Kirane, S. Ghosh, A cold dwell fatigue crack nucleation criterion for polycrystalline Ti-6242 using grain-level crystal plasticity FE model, Int. J. Fatigue 30 (2008) 2127–2139.
- [29] C.L. Xie, S. Ghosh, M. Groeber, Modeling cyclic deformation of HSLA steels using crystal plasticity, ASME J. Eng. Mater. Technol. 126 (2004) 339–352.
- [30] S. Sinha, S. Ghosh, Modeling cyclic ratcheting based fatigue life of HSLA steels using crystal plasticity FEM simulations and experiments, Int. J. Fatigue 28 (2006) 1690–1704.
- [31] T.J.R. Hughes, *The Finite Element Method: Linear Static and Dynamic Finite Element Analysis*, Dover, Mineola, N. Y., 2000.
- [32] K.J. Bathe, *Finite Element Procedures*, Prentice Hall, 1995.
- [33] I.I. Blekhman, *Vibrational Mechanics*, World Scientific, 2000.
- [34] J.J. Thomsen, *Vibrations and Stability: Theory, Analysis and Tools*, Springer-Verlag, Berlin, 2004.
- [35] C. Oskay, J. Fish, Multiscale modeling of fatigue for ductile materials, Int. J. Multiscale Comput. Eng. 2 (2004) 1–25.
- [36] Q. Yu, J. Fish, Temporal homogenization of viscoelastic and viscoplastic solids subjected to locally periodic loading, Comput. Mech. 29 (2002) 199–211.
- [37] S. Manchiraju, M. Asai, S. Ghosh, A dual time scale finite element model for simulating cyclic deformation of polycrystalline alloys, J. Strain Anal. Eng. Des. 42 (2007) 183–200.
- [38] S. Balasubramanian, L. Anand, Elasto-viscoplastic constitutive equations for polycrystalline fcc materials at low homogeneous temperatures, J. Mech. Phys. Solids 50 (2002) 101–126.
- [39] R.J. Asaro, J.R. Rice, Strain localization in ductile single crystals, J. Mech. Phys. Solids 25 (1977) 309–338.
- [40] J. Harder, Crystallographic model for the study of local deformation processes in polycrystals, Int. J. Plast. 15 (1999) 605–624.
- [41] R.J. Morrissey, D.L. McDowell, T. Nicholas, Microplasticity in HCF of Ti-6Al-4V, Int. J. Fatigue 23 (2001) S55–S64.
- [42] C.H. Goh, J.M. Wallace, R.W. Neu, D.L. McDowell, Polycrystal plasticity simulations of fretting fatigue, Int. J. Fatigue 23 (2001) 5423–5435.
- [43] C.H. Goh, R.W. Neu, D.L. McDowell, Crystallographic plasticity in fretting of Ti-6Al-4V, Int. J. Plast. 19 (2003) 1627–1650.
- [44] C.L. Chow, Y. Wei, A model of continuum damage mechanics for fatigue failure, Int. J. Fract. 50 (1991) 301–316.
- [45] M.H.J.W. Paas, P.J.G. Schreurs, W.A.M. Berkelmans, A continuum approach to brittle and fatigue damage: theory and numerical procedures, Int. J. Solids Struct. 30 (1993) 579–599.
- [46] J. Fish, Q. Yu, Computational mechanics of fatigue and life predictions for composite materials and structures, Comput. Methods Appl. Mech. Eng. 191 (2002) 4827–4849.
- [47] C. Oskay, J. Fish, Fatigue life prediction using 2-scale temporal asymptotic homogenization, Int. J. Numer. Methods Eng. 61 (2004) 329–359.
- [48] S. Manchiraju, K. Kirane, S. Ghosh, Dual-time scale crystal plasticity FE model for cyclic deformation of Ti alloys, J. Comp. Aid. Mater. Des. 14 (2008) 47–61.
- [49] J.S. Walker, *A primer on wavelets and their scientific applications*, CRC Press, 1999.
- [50] G. Strang, T. Nguyen, *Wavelets and Filter Banks*, Wellesley College, 1996.
- [51] A. Jensen, A.L. Cour-Harbo, *Ripples in Mathematics, the Discrete Wavelet Transform*, Springer, 2001.
- [52] M.A. Crisfield, *Non-linear Finite Element Analysis of Solids and Structures*, Academic Press, 1996.